Computational Modelling and Treatment Optimization of Acute Endovascular and Respiratory Conditions

by

Tom Dillon

B.E. Mechanical Eng., National University of Ireland, Galway (2018)
M.E. Electronic Eng., National University of Ireland, Galway (2019)

Submitted to the Department of Mechanical Engineering
in partial fulfillment of the requirements for the degree of

Master of Science in Mechanical Engineering

at the

MASSACHUSETTS INSTITUTE OF TECHNOLOGY

June 2021

Author .....
Department of Mechanical Engineering
May 14, 2021

Certified by .....
Ellen T. Roche
Associate Professor
Thesis Supervisor

Accepted by .....
Nicolas Hadjiconstantinou
Chairman, Department Committee on Graduate Theses

Computational Modelling and Treatment Optimization of Acute Endovascular and Respiratory Conditions

by

Tom Dillon

Submitted to the Department of Mechanical Engineering
on May 14, 2021, in partial fulfillment of the
requirements for the degree of
Master of Science in Mechanical Engineering

Abstract

This thesis aims to use computational tools and a deterministic clinical design process to optimize treatment for acute endovascular and respiratory conditions. Specifically, focus is placed on optimizing treatment for two acute pathologies: (1) the Coronavirus disease 2019 (COVID-19), and (2) Abdominal Aortic Aneurysms (AAA).

In light of the recent COVID-19 pandemic, a low-cost, rapidly deployable emergency ventilator design using a novel fluidic oscillator was developed. The design addresses potential ventilator shortages resulting from the ongoing and future pandemics by converting a continuous positive airway pressure (CPAP) machine into a mechanical ventilator using a part that is (i) inexpensive, (ii) easily manufactured without the need for specialized equipment, (iii) simple to assemble and maintain, (iv) does not require any electronics, and (v) has no moving components that could be prone to failure. A Computational Fluid Dynamics (CFD) model was used to assess flow characteristics of the system, and a prototype was developed and tested with a commercial benchtop respiratory simulator. The simulations showed clinically relevant periodic oscillations and outlet pressures between 8-23 cm H_2O. Both the prototype and simulations responded promptly to disrupted oscillations, an analogue for patient-initiated breaths.

AAA is a swelling in the lower portion of the aorta, the largest blood vessel in the body. The incidence of this potentially fatal condition is 5-10 cases per 100,000 in the U.S.. The preferred treatment for AAA is minimally invasive endovascular repair (EVAR), whereby a compliant tubular material reinforced with a metallic stent (an endograft) is implanted inside the aneurysm. For aneurysms that extend across major abdominal vessels (juxtarenal aneurysms), a fenestrated (or sub-branched) endograft is required. The lead time to obtain a patient-specific fenestrated graft from a commercial manufacturer is in the order of a few weeks, which is often unsuitable for patients that present with an emergent medical condition. Physicians instead choose mostly to manually modify off-the-shelf non-fenestrated endografts, though this process is often tedious and subject to calculation inaccuracies. In this thesis, a computer program for automated fitting of fenestrations on non-fenestrated endo-

grafts is proposed - "FenFit". FenFit provides the physician with an efficient, intuitive user interface for modifying endovascular grafts, developed using MATLAB GUI designer. A novel search algorithm using 3D to 2D projection mapping was developed to determine the optimal placement of fenestrations on the endograft at reduced computational cost, and a bijective conformal mapping algorithm was developed for texture mapping of the fenestrations to the 3D aortic graft space. A pilot clinical study was conducted in conjunction with our collaborators at Beth Israel Deaconess Medical Center (BIDMC), Boston, to evaluate the efficiency of FenFit against physician manual planning. Results to date have shown that FenFit can reduce workflow planning time from 22.5 minutes to 32 seconds ($n = 25$, $p < 0.001$). In 20% of cases, FenFit found a valid graft alignment where the physician could not via trial and error.

Guided by computational tools, these combined bodies of work propose expedited, patient-specific treatment for urgent medical conditions. It is hoped that these accelerated treatment regimes may ultimately translate to improved clinical outcomes for the patient.

Thesis Supervisor: Ellen T. Roche
Title: Associate Professor

Acknowledgments

Firstly, I would like to extend my warmest thanks to my advisor Prof. Ellen Roche for giving me the opportunity to work in her lab, and for her constant engagement and mentoring throughout my Master's journey. I have thoroughly enjoyed my time working in the TTDD lab, and I'm excited to see what the next few years here will bring.

I would like to thank Dr. Patric Liang and Dr. Marc Schermerhorn from Beth Israel Medical Center Boston for their constant input and endless patience throughout the development of the FenFit program. As busy clinicians, they always made time for describing clinical problems, trialling software in the OR, and offering continuous feedback - something I have valued very highly.

I also want to thank all of my labmates/friends in the MIT TTDD lab. I am constantly inspired by their astounding research, generosity, and willingness to offer help at every turn. Thanks also to my friends in MechE that have made my experience here so enjoyable - I'll never forget the hikes, snowboarding trips, runs by the Charles, and acro-yoga sessions on Killian!

Last but not least, I would like to thank my Mom, Dad, and sisters Rebecca, Rachael, and Emma, for their constant love and support since moving to the US. I would not have been able to accomplish the work in this thesis without them.

Contents

List of Figures

Chapter 1

Introduction

This thesis describes the use of computational modeling and deterministic design to improve patient healthcare in the context of acute endovascular and respiratory conditions. Specifically, focus is placed on optimizing treatment for two acute pathologies: (1) the Coronavirus disease 2019 (COVID-19), and (2) Abdominal Aortic Aneurysms (AAA).

The first project is concerned with the development of a novel fluidic oscillator design for conversion of standard continuous positive airway pressure machines to emergency-use mechanical ventilators in light of the COVID-19 pandemic. Research for this project began in April 2020, when there was a serious concern regarding the insufficient supply of ventilators to support critically ill patients. As will be demonstrated, emphasis in this thesis is placed on expedited manufacture and use of medical devices. This is achieved through an understanding of workflow and mechanics of existing systems, which is crucial in promptly addressing acute and emergent medical conditions.

The second project presented in this thesis concerns the design of a computational program for automated fenestration fitting in the design of endografts (i.e. artificial blood vessels placed inside existing vessels) for use in aortic aneurysm surgery. An aneurysm is the swelling or dilation of a blood vessel, and a fenestration is a hole or sub-branch placed on an endograft to maintain the patency (i.e. the openness) of the vessel to maintain blood flow to various organs. A clear clinical need was identified

through close interaction with our group's clinical collaborators, who complained that the current workflow for planning AAA intervention is tedious and occasionally unreliable. The goal of this research was to automate the design of fenestrated aortic endografts, increasing both the efficiency and accuracy of aneurysm surgical planning.

1.1 Design Process and Thesis Summary

This thesis is focused on the translation of clinician and patient needs to quantitative functional requirements that drive the design and modeling process. The general workflow implemented in both projects is highlighted in Figure 1-1.

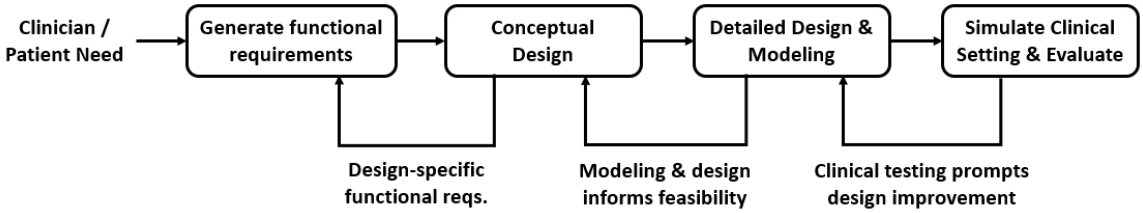

Figure 1-1: Clinical design workflow implemented throughout this thesis.

Consideration is given at all levels of design for clinicians that interact with the technologies presented, and patients that receive their corresponding treatments.

An overview diagram of this thesis is shown in Figure 1-2. Computational modeling and design of a novel fluidic oscillator for use in emergency mechanical ventilators is highlighted in Chapter 2. An automated computer program for fenestration fitting is highlighted in Chapter 3, and 3D visualization of results obtained from this program are discussed in Chapter 4. Finally, conclusions and scope for future work for both projects are outlined in Chapter 5.

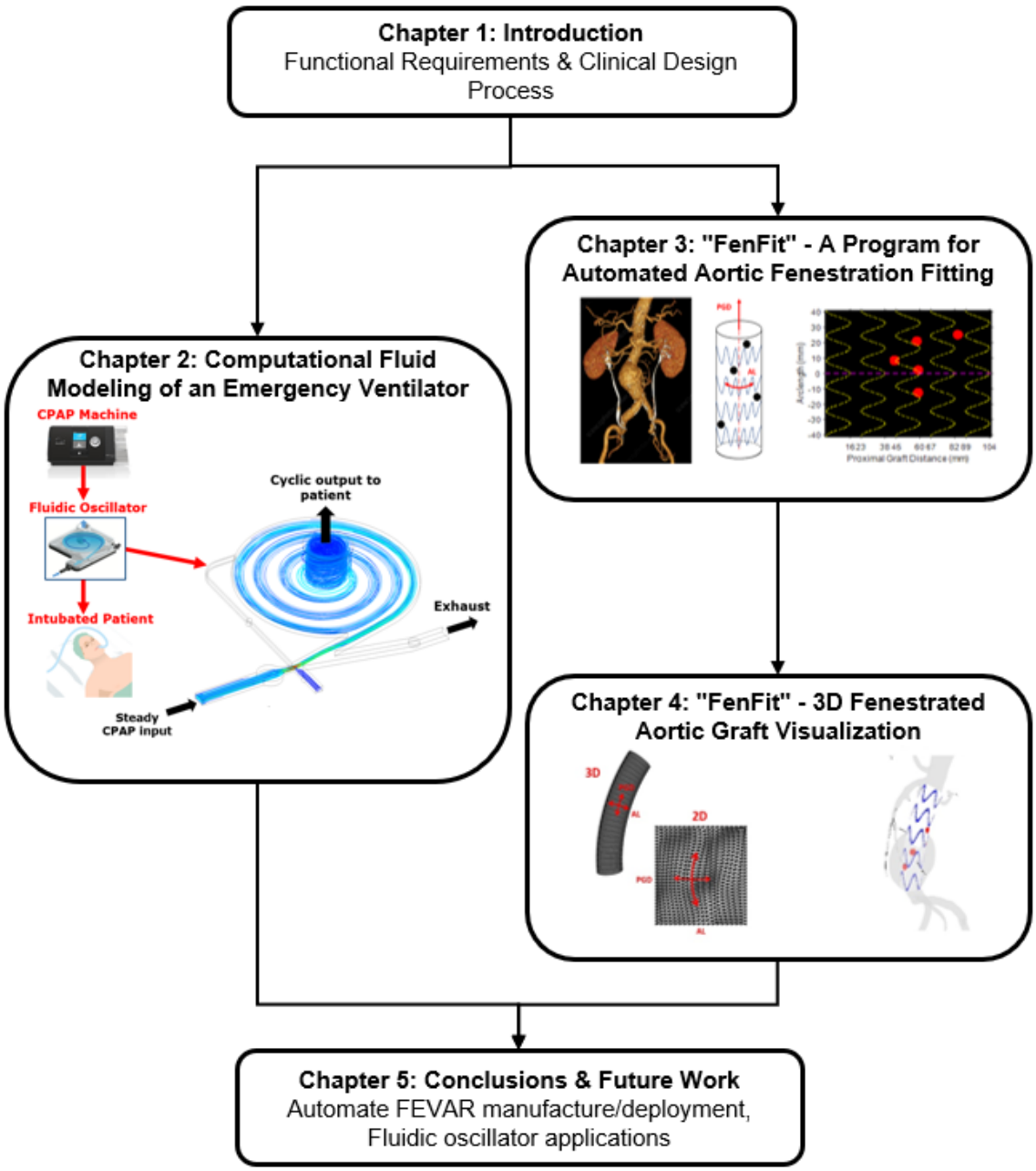

Figure 1-2: Thesis Overview.

Chapter 2

Computational Fluidic Modeling and Design of a Low-Cost, Emergency Use Mechanical Ventilator

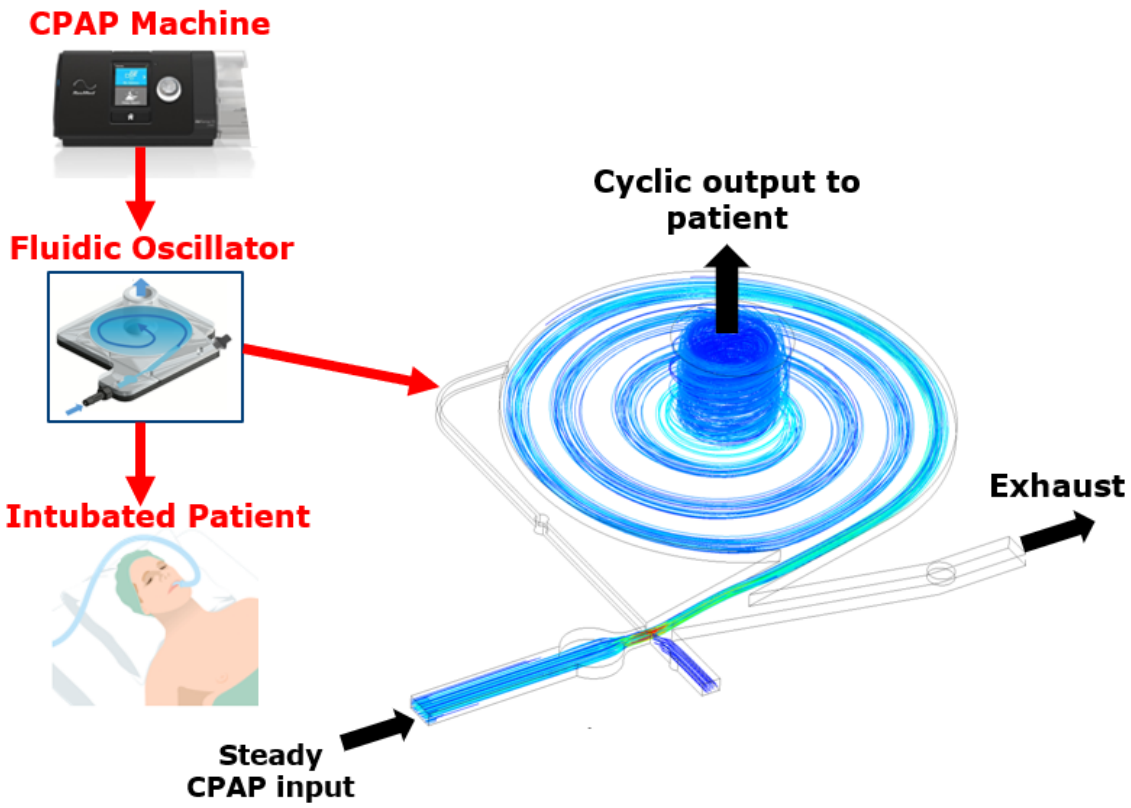

This chapter presents the computational fluidic modeling of a fluidic oscillator for the conversion of continuous positive airway pressure (CPAP) machines into emergency pressure support mechanical ventilators by providing a periodic pressure output to patients. The design addresses potential ventilator shortages resulting from the COVID-19 pandemic, or future pandemics by converting a positive pressure source into a mechanical ventilator with a part that is (i) inexpensive, (ii) easily manufactured without the need for specialized equipment, (iii) simple to assemble and maintain, (iv) does not require any electronics, and (v) has no moving components that could be prone to failure. A Computational Fluid Dynamics (CFD) model was used to assess flow characteristics of the system, and a prototype was manufactured and tested with a commercial benchtop respiratory simulator. This chapter is based on work published in Advanced NanoBiomed Research, "Computational Fluidic Modeling of a Low-Cost Fluidic Oscillator for Conversion of a CPAP Machine into an Emergency Use Mechanical Ventilator" [47].

2.1 Introduction and Background

The coronavirus disease 2019 (COVID-19) pandemic has placed a tremendous burden on the healthcare system worldwide. At the beginning of the pandemic, there was a very serious concern regarding the insufficient supply of ventilators to support critically ill patients. In the United States, a country that spends 18% of GDP on annual health expenditures – more than twice the average among developed countries – it was estimated that there would be a shortage of at least 45,341 ventilator units during the first peak of the outbreak [5]. Although this shortage did not transpire, there could still be a need for emergency ventilators during this pandemic, or indeed in future pandemics. While vaccines are being rolled out, there remains a potential need for more ventilator units. This need is particularly pressing in developing countries where resources are less abundant, vaccines may not be imminently available and ventilator cost is prohibitive; it was reported in May 2020 that there are at least ten countries in Africa that have no ventilators [20].

To meet demand for emergency ventilators in a timely and cost-efficient manner,

fluidic oscillators can be utilized as a means to convert continuous positive airway pressure (CPAP) machines into ventilators. Fluidic oscillators are based on the bi-stable states of a jet of fluid inside a specifically designed flow chamber, and can be harnessed to produce self-excited oscillating fluid flow. Combined with a CPAP machine - of which there are millions available in the United States alone - fluidic oscillators can be used to create functional emergency use ventilators without the need for complex moving parts [44]. The A.R.M.E.E (Automatic Respiration Management Exclusively for Emergencies) utilizes one such device, based on a fluidic oscillator developed by the US Army in 1965 [19], as illustrated in Figure 2-1.

However, the A.R.M.E.E. device is limited to a maximum oscillation period of 1 second, which limits the minimum achievable respiratory rate, a crucial metric used by physicians to manage patients on mechanical ventilation [19]. Key functional requirements for the oscillator were defined as follows:

- Oscillation range between 3-6 seconds (i.e. respiratory rate (RR) or 10-20 breaths per minute (bpm)).

- Output ventilation with positive end expiratory pressures (PEEP) in the range of 8-12 cmH_2O, and peak inspiratory pressures (PIP) between 18-23 cmH_2O.

Other design specifications include no moving parts or electronics (such that the design can be manufactured and deployed at low cost, even in developing countries), and an adjustable oscillation period and amplitude.

In this chapter, the design, modeling, fabrication and testing of an alternative fluidic oscillator design capable of the above specifications is presented. The clinical metrics outlined above fall within the guideline recommended ranges for emergency use ventilators to treat patients with COVID-19 respiratory failure [39]. Our design, which affords physicians greater control over respiratory rate compared to currently available fluidic oscillator approaches for mechanical ventilation, can be rapidly manufactured to meet the pressing demand during this global pandemic and beyond.

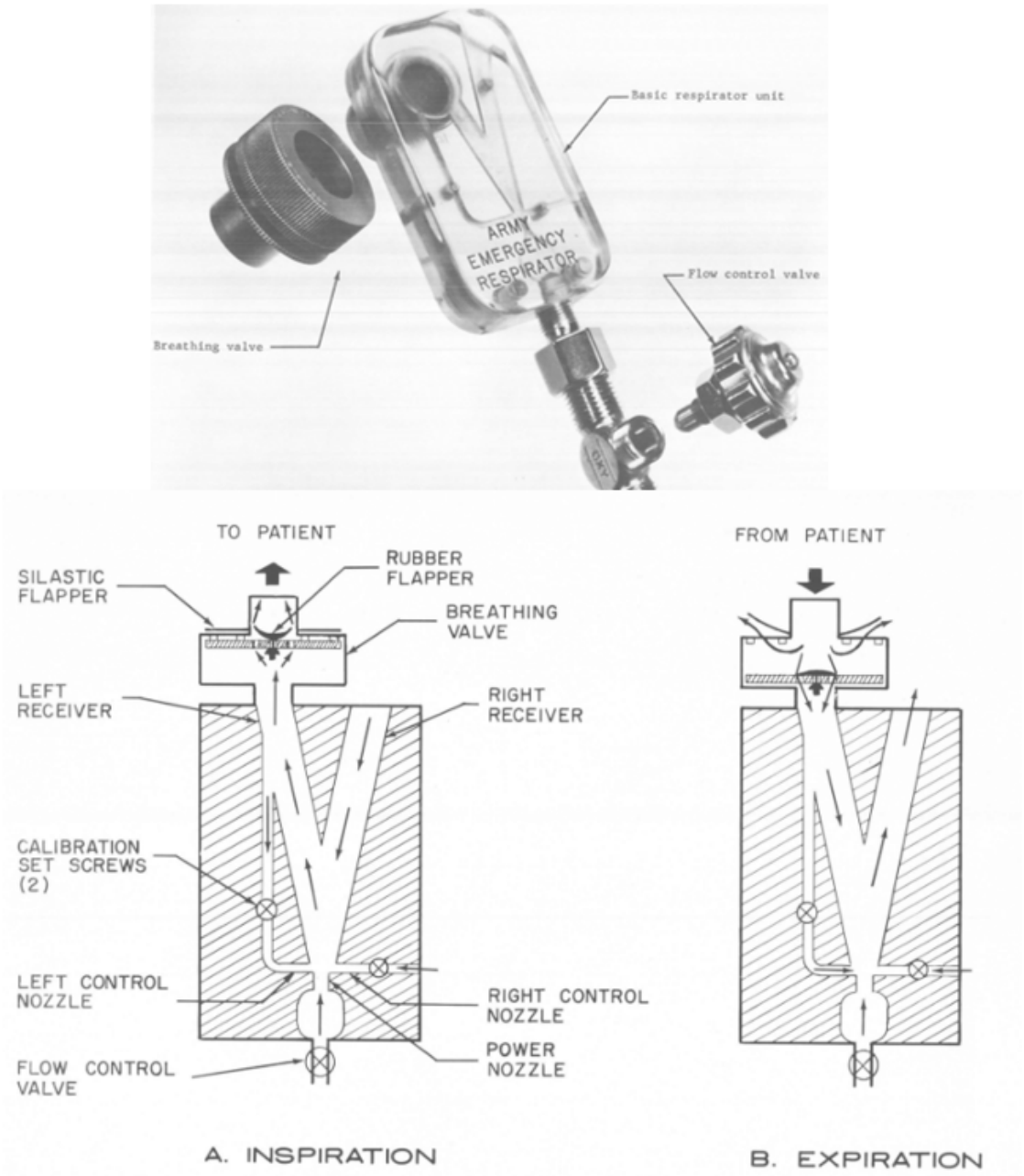

Figure 2-1: The A.R.M.E.E. ventilator monostable fluidic oscillator design (top) as illustrated in 1965 US Research Patent [19]. The operational concept of the device is highlighted during inspiration (bottom left) and expiration (bottom right).

2.2 Conceptual Design

The overall concept for the CPAP-ventilator conversion is highlighted in Figure 2-2. As mentioned previously, for our design to be clinically applicable, we targeted oscillation periods on the order of 3-6 seconds (RR 10-20 bpm) according to the consensus guidelines for emergency use ventilators [39]. The switching time for an oscillator is related to the characteristic time of the vortex chamber; that is, the time taken to fill the vortex chamber with fluid for a given mass flow rate:

$$\Delta t_c = \frac{\pi D^2 h}{4 v \dot{m}} \tag{2.1}$$

where Δt_c is the characteristic time, D and h are the diameter and height of the vortex chamber, respectively, v is the specific volume of the fluid, and $\dot{m}$ is the mass flow rate [48]. To improve upon the A.R.M.E.E. ventilator oscillation period of 1 second, a larger vortex chamber (88 mm vs. 22 mm) was implemented. The height of the vortex chamber is relatively small (2.4 mm), which serves to maintain adequate pressures at the patient outlet. An input flow rate of 30 L/min was selected based on standard CPAP specifications for treating patients with COVID-19 respiratory failure [39]. Critical dimensions for the oscillator can be found in Appendix A.

The nozzle-diverter region exploits the Coanda effect (the tendency of a fluid to remain attached to walls), so that nozzle flow is not divided between the patient and exhaust outlets throughout the respiratory cycle, but instead oscillates from one to the other [48, 18]. The high-velocity, low-pressure air in the feedback channel (FC) pulls nozzle flow towards the vortex chamber during the inspiration (Figure 2-2). This feedback loop serves the purpose of transporting a small portion of the outflow back to the nozzle-diverting region to create the desired return flow behavior between the vortex chamber and exhaust channel (EC). At the end of inspiration when the lungs are expanded, the pressure increase drives the flow switch at the nozzle-diverter region from the vortex chamber (patient output) to the exhaust channel, initiating exhalation (Figure 1B). Air is pulled from the patient, through the vortex chamber,

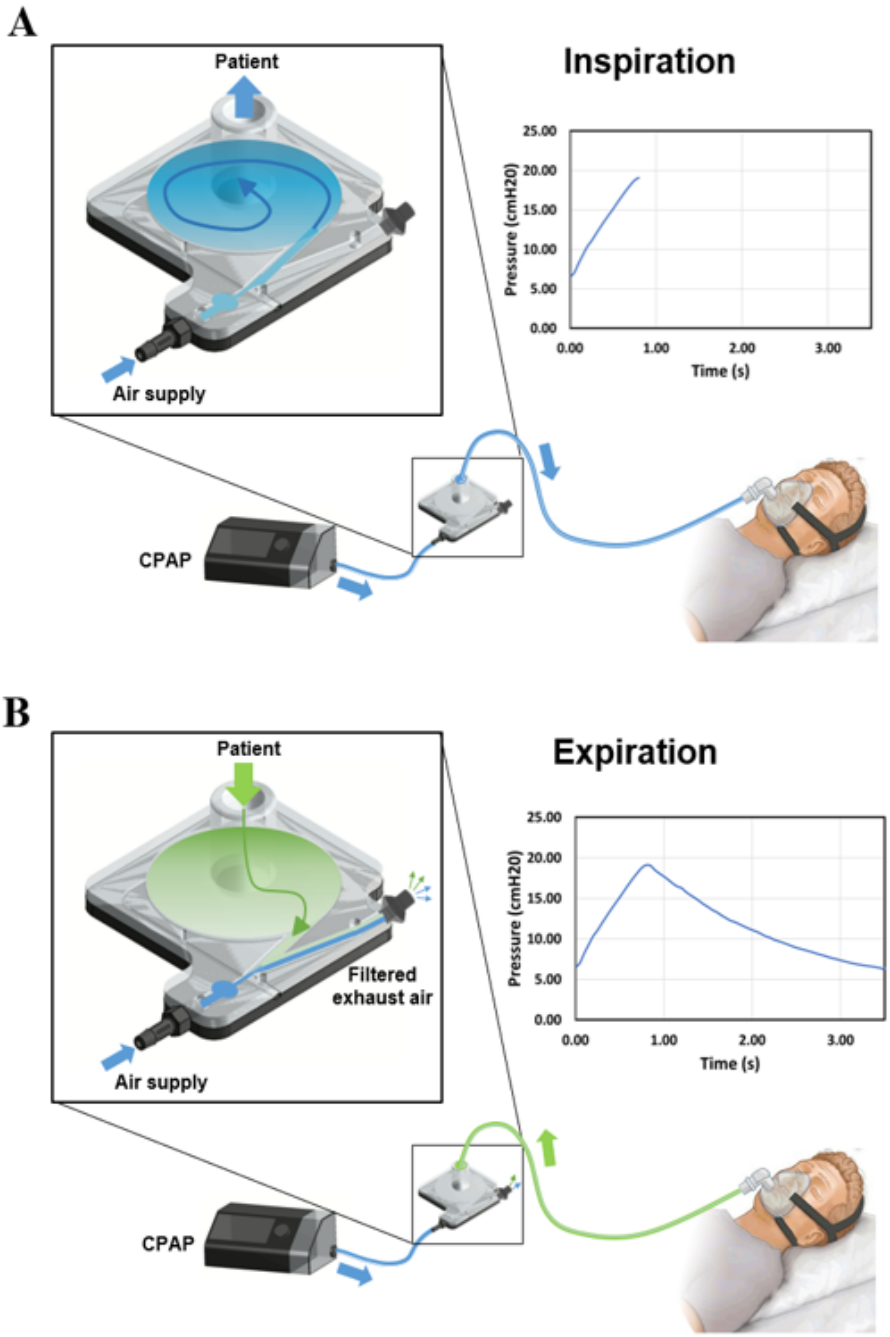

Figure 2-2: Converting a standard CPAP machine for pressure-controlled mechanical ventilation through implementation of a novel fluidic oscillator design. During inspiration, air flows from the CPAP machine, through the oscillator, and into the patient's lungs. Accumulation of air inside the lungs causes a corresponding increase in alveolar pressure (A). During expiration, flow reverses out of the patient's lungs through the oscillator, exiting the system through a filtered exhaust. Deflation of the lungs results in a corresponding decrease in alveolar pressure (B)

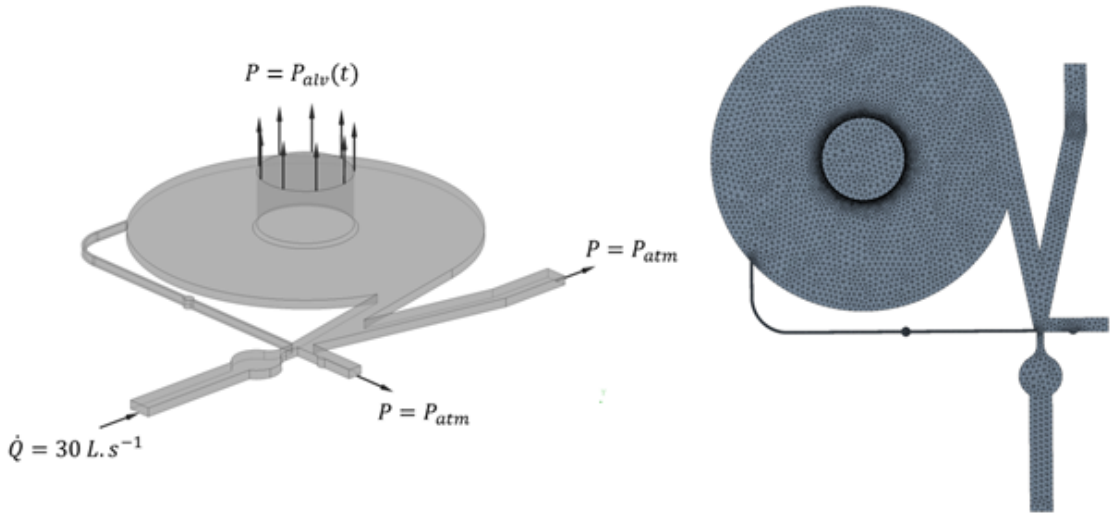

Figure 2-3: Boundary conditions (left) and mesh (right) applied for the fluidic domain CFD model.

and out through the exhaust channel, marking the exhalation phase of the respiratory cycle. The side channel (SC) pressure remains constant throughout the respiratory cycle, which provides more stable Peak Inspiratory Pressures (PIP) and Positive End Expiratory Pressures (PEEP). The three set-screws on the FC, SC, and EC are used to calibrate the oscillator (discussed in detail in section 2.5).

2.3 Model Setup

ANSYS Fluent software was used to conduct a Computational Fluid Dynamics (CFD) analysis of the oscillator. A k- turbulence model was selected, owing to its capability of capturing adverse pressure gradients and turbulent dissipative effects [14]. The mesh geometry contained more than 170,000 tetrahedral elements. A flow rate of 30 L/min was applied at the CPAP inlet, and the SC and EC outlets were set to atmospheric pressure. A no-slip condition was defined at the oscillator walls. The convergence criterion for the residuals of mass, momentum, and energy equations was set to 10-4 for each simulation. The physical quantities such as pressure, flow rate, and velocity were also monitored for the convergence. An illustration of both the mesh and boundary conditions utilized are illustrated in figure 2-3.

A first-order *RC* Windkessel model, which describes the lungs as a resistance

element, R, connected in series with a capacitance element, C, was implemented to capture the variation in alveolar pressure over the respiratory cycle. The alveolar and pleural pressures, are strongly coupled with the dynamics of the oscillator [1], as described in Equation 2

$$P_{alv}(t) = \dot{Q}R + \frac{1}{C}\int_0^{\Delta t} Q dt + P_{peep} + P_{pl} \tag{2.2}$$

where P is pressure, t is time, C and R are lung compliance and resistance, respectively ($C = 30$ ml/cmH_2O, $R = 3$ cmH_2O/L/s, according to clinical data from patients with COVID-19 [10, 25]), and Q is flow, and the subscripts alv, $peep$, and pl denote alveolar, PEEP, and pleural pressures, respectively. Implementation of the coupled fluidic RC circuit equivalent is depicted in Figure 2-4.

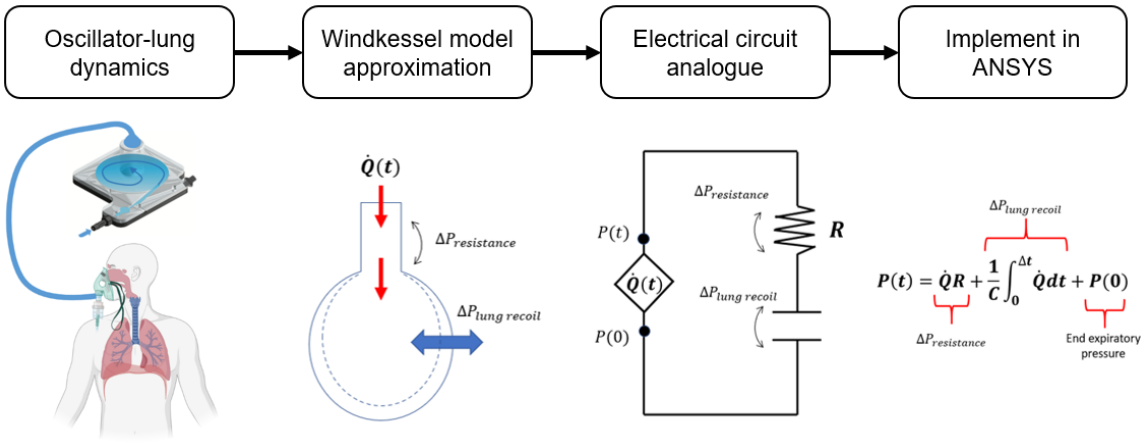

Figure 2-4: Coupled simulation workflow using the 2-element Windkessel model.

2.4 Initial Results

Figure 2-5 illustrates the CFD results at different stages throughout the respiratory cycle. At the beginning of inspiration, alveolar pressure is relatively low, and air circulates inside the vortex chamber before entering the lungs (Stage I). Eventually, high pressure stagnation inside the chamber causes nozzle flow to switch over to the exhaust side (Stage II). Following the switch, high pressure air is expelled from the lungs, returning along its inspiratory path through the oscillator and exits the system through the exhaust which a filter would be applied (Stage III). At the end of expiration, lung pressure is low, prompting flow to switch back to the patient inlet (Stage IV), beginning the respiratory cycle again.

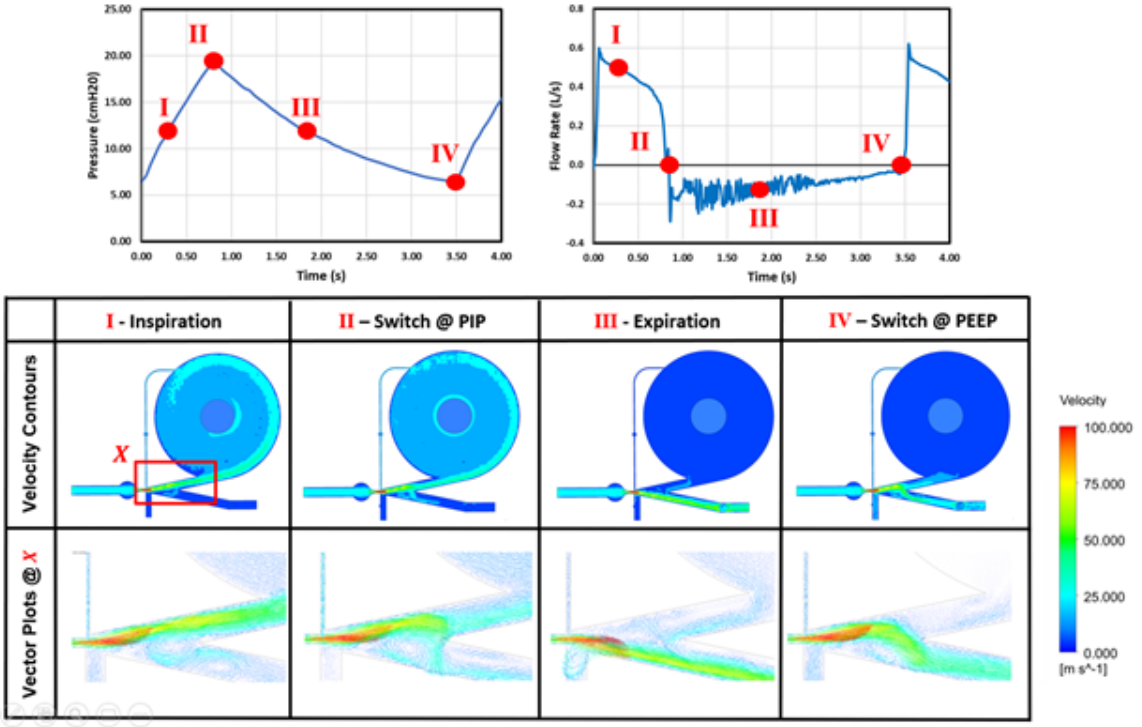

Figure 2-5: Velocity contours vector plots (table), with associated pressure (graph, left) flow rate (graph, right) profiles, taken at different stages throughout the respiratory cycle (I-IV).

Key design parameters were investigated and used in an iterative design process to optimize performance. This was carried out by adjusting parameters such as the vortex chamber height and diameter, and feedback channel dimensions. We assessed the

outcomes of these adjustments by both continuously monitoring key clinical performance variables during simulation (PIP, PEEP, and RR), and qualitatively analyzing the corresponding 3D flow streamlines (e.g. switching behavior of the flow, vortex chamber turbulence, feedback channel flow, etc.). A sample snapshot of these flow streamlines can be seen in Figure 2-6.

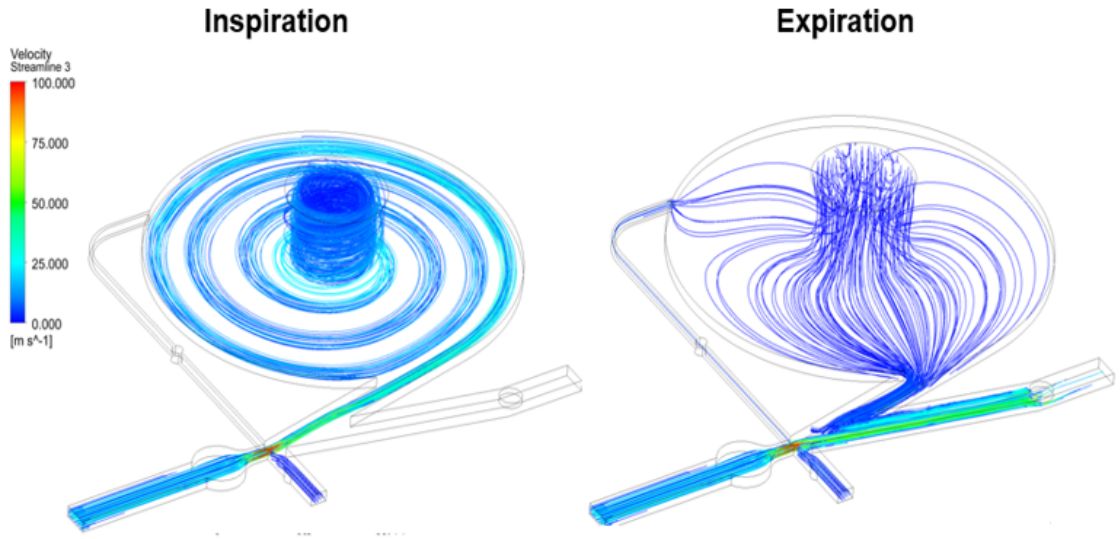

Figure 2-6: Streamline velocity results for the oscillator during inspiration and expiration, marked respectively as I and III in Figure 2-5.

2.5 Patient Considerations

The following section describes functional parameter tuning in silico. Figures 2-7 and 2-8 demonstrate an inspiration to expiration ratio (I:E) that varies between 1:2 and 1:5, with clinically relevant PEEP and PIP values of 8 cmH2O and 20 cmH2O, respectively. The purpose of this section is to show that the design's performance can be continuously varied across this range of values to match the oscillator's output to the appropriate level of respiratory assistance required by the patient.

2.5.1 Pressure Amplitude and Period Variation

As mentioned previously, an adjustable RR of 10-20 breaths per minute was identified as a key design criterion for the oscillator [39]. A grub screw at the EC (highlighted in Figure 2-7) was implemented to allow tunability of the RR, under the assumption that obstructing the exhaust channel could facilitate slower 'drainage' of the device during expiration. The effect of EC screw depth on the oscillation period was studied in the CFD model. As seen in Figure 2-7, increasing the EC screw depth reduced the rate of pressure decay between PIP and PEEP, facilitating an adjustable oscillation period of 3-5 seconds (RR 12-20 breaths per minute). A positive linear relationship was observed between exhaust screw depth, d, and oscillation period, T where $T = 7.6d - 4.7$, where $R^2 = 0.98$. Variations in PIP and PEEP under different EC screw depths were found to be 1 cmH_2O and 3 cmH_2O, respectively, which are small relative to the overall oscillation amplitude of 13 cmH_2O. Hence, the EC screw allows for robust, predictable control of the oscillation period.

The other two set-screws on FC and SC were utilized to enable adjustments in PEEP and PIP. Control of PIP is paramount for pressure-controlled ventilation, as elevated values may increase the risk of mechanically-induced barotrauma [39, 37]. CFD analysis was conducted to determine the effects of the FC and SC depth on PIP. Figure 2-7 demonstrates that the simultaneous opening of the FC screw and closing of the SC screw increases PIP.

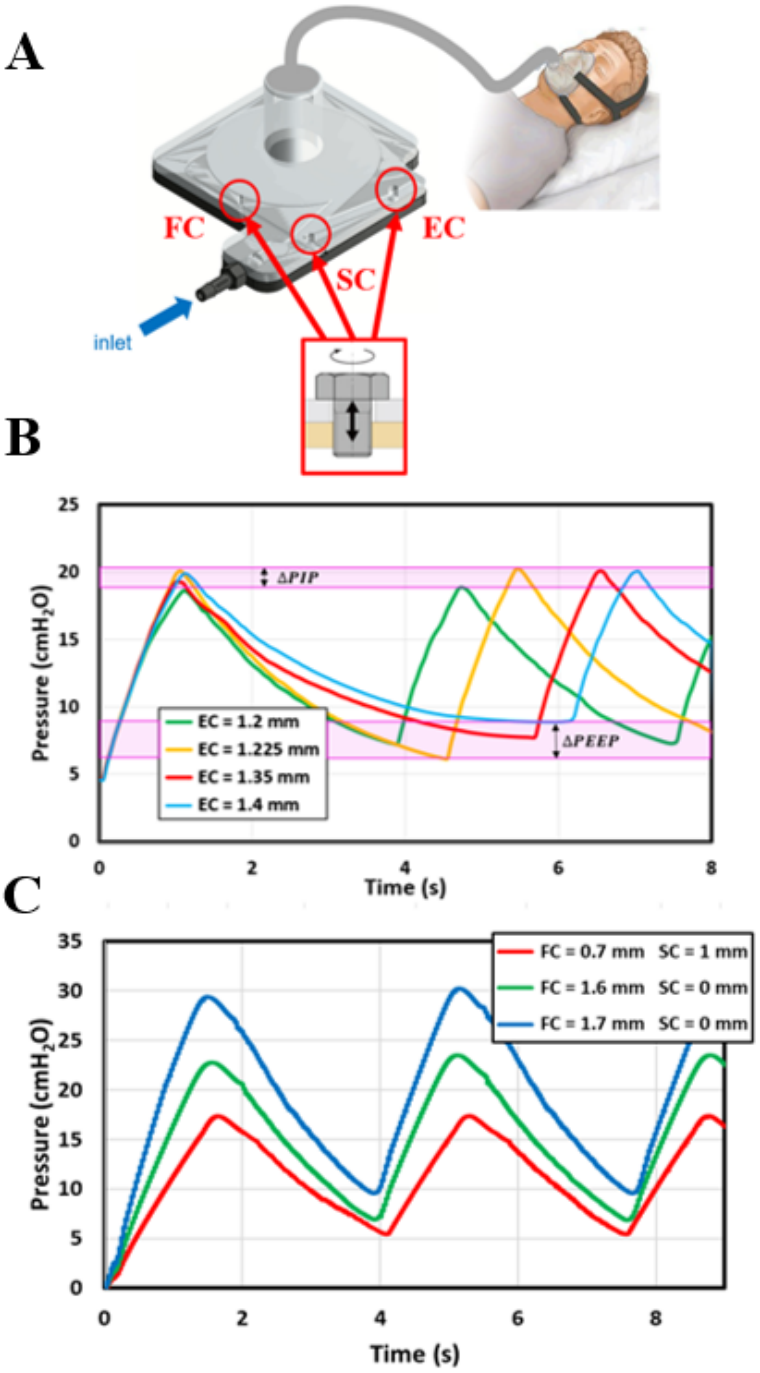

Figure 2-7: Functional parameter tuning *in silico*. Illustration of the Exhaust Channel (EC), Feedback Channel (FC), and Side Channel (SC) screw locations referenced in this figure (A). Variation in oscillation period for a selection of EC screw depths (B). PEEP and PIP ranges are indicated on the graph also. Tuning PIP and PEEP through simultaneous variation of FC and SC screw depth (C).

2.5.2 Patient Triggering

Patient discomfort can arise when a delay exists between the desire to inhale, and the oscillator's switchover to inspiration. The patient's intention to inhale is detected in modern ventilators by a moderate decrease in alveolar pressure (i.e. a pressure trigger) [39, 7, 13]. If the ventilator does not respond to this trigger, the patient will take a breath later than they are comfortable with. The active pressure component contributed by the patient is represented in Equation 2.2 by the pleural pressure, P_{pl}. Here, the patient trigger is modeled as a forced step function of magnitude -3 cmH2O with first-order dynamics and the time constant τ, defined as $\tau = RC$ [38]. The effects of triggering on the oscillator's dynamics during the expiration phase were characterized, and the results are presented in the following sections.

Figure 2-8 illustrates that the oscillation period can vary dynamically from cycle to cycle based on a patient trigger. The data corroborates that a premature transition from the expiratory phase to the inspiratory phase is possible following a small decrease in alveolar pressure, representing a patient-initiated breath. In the cycle immediately following the trigger, PIP, PEEP, and oscillation period all remain consistent.

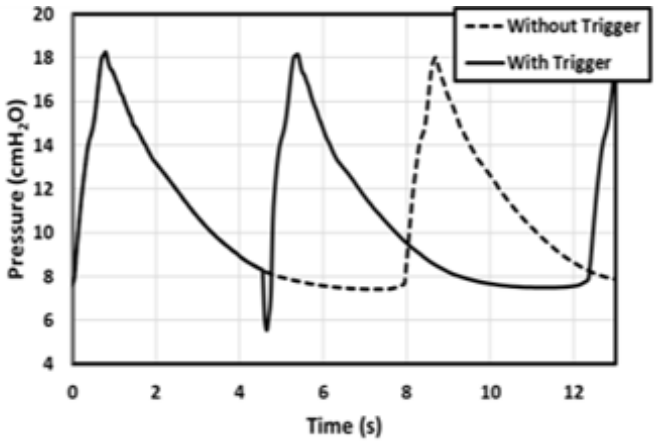

Figure 2-8: Controlling the oscillation period in response to a patient trigger. Note the small decrease in pressure at 4.5s induced by the patient.

2.6 Manufacture and Experimental Testing

A prototype of the oscillator was developed, consisting of three layers of laser-cut scratch- and UV-resistant cast acrylic sandwiched together. The central layer (2.4 mm thickness) contains the main oscillator geometry, and the top and bottom layers (3.2 mm thickness) are sealed using clear fast cure epoxy (J-B Weld). A 3D printed connector was attached to an opening in the top layer above the vortex chamber, which was in turn connected to the ASL 5000 Breathing Simulator. An additional 3 openings were cut above the FC, SC and EC channels, and screws for variable occlusion were placed into each (Figure 2-9. These screws are used to alter flow resistance as predicted in silico.

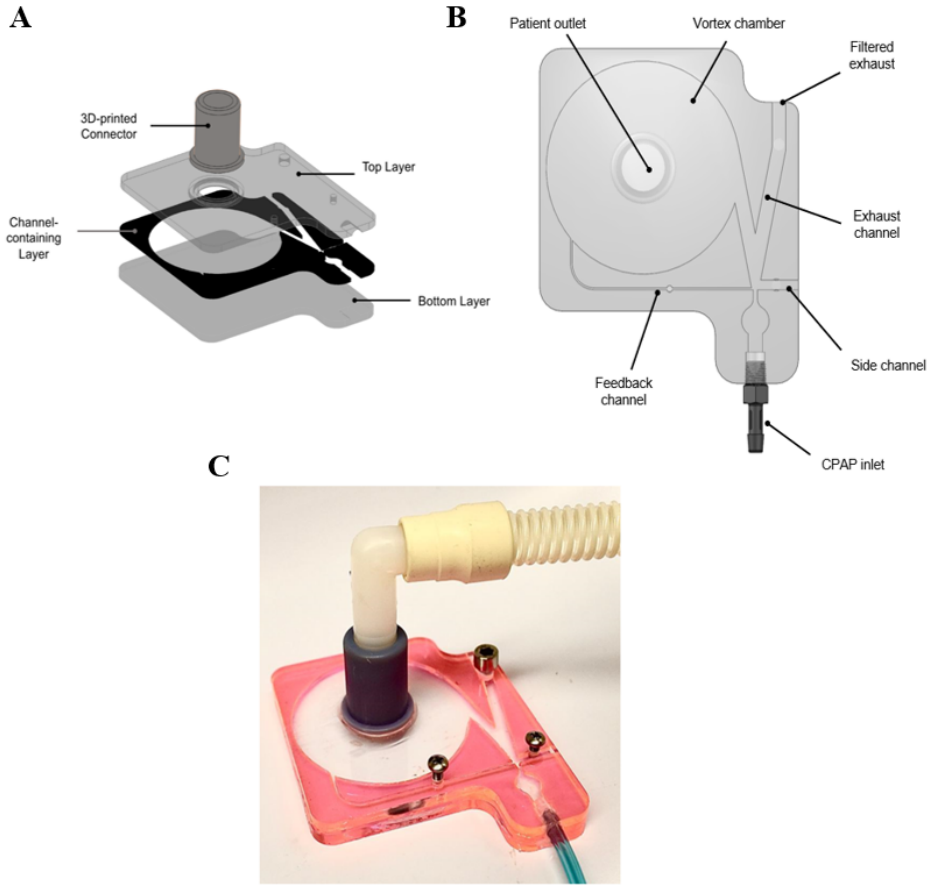

Figure 2-9: Oscillator assembly consisting of 3 layers of laser-cut acrylic and a 3D printed connector (A). Plan view of the novel oscillator design (B), and final prototype including channel occlusion screws (C).

Tests on the respiratory simulator - ASL 5000 Breathing Simulator (IngMar Medical) - were conducted with a constant input flow rate of approximately 30 L/min measured using a digital mass flow meter (SFM300, Sensirion). Pressures and volumes were recorded directly by the ASL simulator. A muscle (diaphragmatic) pressure profile simulating a patient-initiated breath every 4 seconds was applied in the ASL settings. To simulate the respiratory mechanics of COVID-19 patients, simulator compliance was varied between 10-50 mL/cmH_2O. COVID-19 causes decreased lung compliance (i.e. stiffening of the lungs) compared to healthy lung compliance of 100-400 mL/cmH_2O [22]. The airway resistance and trigger amplitude were chosen to align with those used in the in silico model (R = 3 cmH_2O/L/s and 5.5 cmH_2O, respectively) [10, 25, 42]. The full experimental setup is shown in Figure A-1.

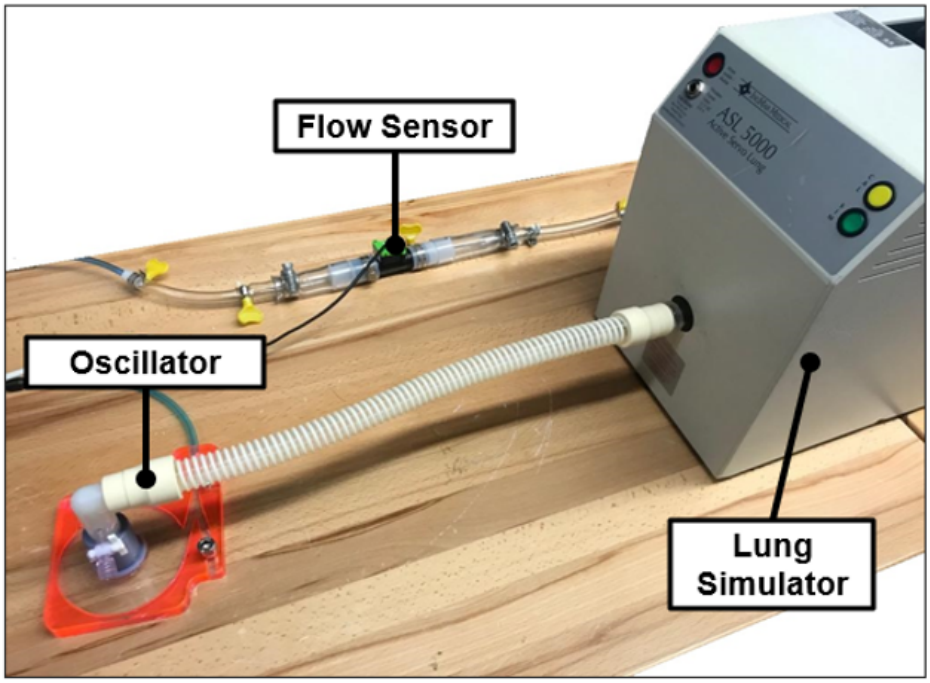

Figure 2-10: ASL Lung Simulator Testing Setup

As illustrated in Figure 2-11, the prototype is able to achieve stable, constant-amplitude oscillations between (11.66 ± 0.37) cmH_2O and (17.15 ± 0.33) cmH_2O at the lung compliances tested (C = 10, 30, 50 ml/cmH_2O, based on the range of lung compliances observed in patients with COVID-19 [10, 25]), with similar waveform shapes to those seen in-silico, and showing minimal variation over a period of

60 seconds (n=15 cycles for each waveform). Moreover, the experimental results demonstrate that the prototype responds successfully to the patient trigger, as inspiration begins immediately following a patient-initiated pressure drop by the lung simulator. Figure 2-11 also demonstrates that the prototype is functional for the range of COVID-19 lung compliances tested, while highlighting that higher compliances produce a slower rate of pressure decay between PIP and PEEP. To account for this effect, the physician can simply vary the EC screw depth as the patient's lung compliance improves or worsens over the course of their intubation period.

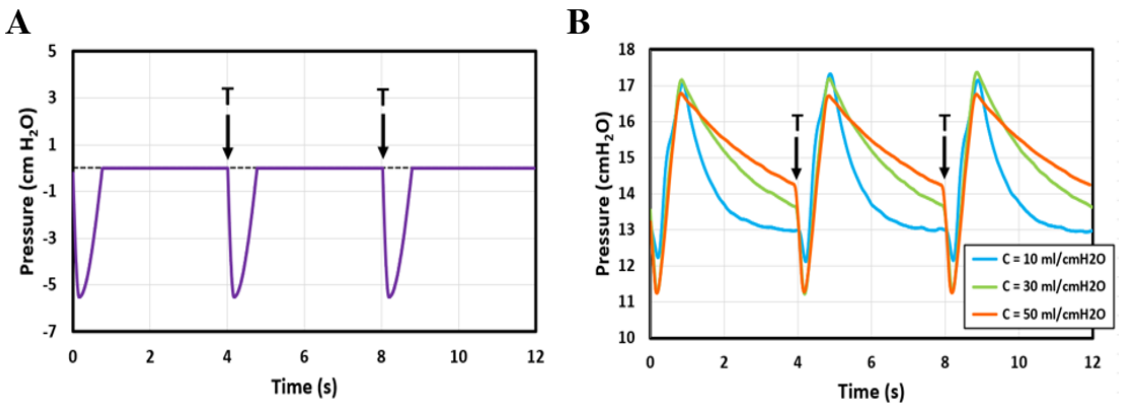

Figure 2-11: The muscle-induced pressure profile applied by the ASL lung simulator to be used for in vitro experimental testing, simulating a patient trigger initiated at regular timepoints T (A). Corresponding experimentally measured pressure profiles for a range of COVID-19 lung compliances from 10-50 ml/cmH2O (B).

2.7 Discussion

The main contributions of this work are as follows; (i) a low-cost fluidic oscillator was presented that is capable of converting a CPAP machine into an emergency use mechanical ventilator, (ii) CFD modeling demonstrated that the design is able to achieve physiologically relevant respiratory pressures and allows greater control of the respiratory rate than previous fluidic oscillator-based solutions, (iii) Using a respiratory simulator, it was shown that a prototype responds successfully to patient-initiated spontaneous breaths, while also remaining functional over a wide range of lung compliances that represent varying levels of lung pathology. Given the aim of this

project was to design an emergency ventilator for under-resourced communities, a key design criterion was simplicity. As such, we sought to avoid complex electromechanical systems that are expensive, potentially difficult to operate, and more prone to failure. Instead, we dedicated our efforts to understanding the oscillator's fluid dynamics using simulation and visualization in CFD. We provide an in-depth explanation of the design's operation at each point throughout the respiratory cycle (see description of Figure 2-5). This knowledge in turn allowed us to better optimize the design, which is evident in the clinically relevant respiratory rates that are achievable (tunable oscillation period between 3-5 s). This represents a substantial improvement on other emergency ventilator designs seen in the literature (such as the emergency A.R.M.E.E. ventilator) that cannot attain the same metrics (maximum 1 s period [19]).

To ensure our simulations most accurately depicted the real-world physics of mechanical ventilation, we coupled a first-order Windkessel model of lung respiratory mechanics to our CFD model that can be adjusted for a range of COVID-19 lung compliances. We provide further quantification of user considerations through implementation of a patient "trigger", which is translated to an induced pressure drop in the Windkessel model. The effect of this trigger was also simulated experimentally, and similar results were obtained to those of the CFD. To the author's knowledge, these modeling approaches have not been applied to CFD simulation of mechanical ventilators to date.

However, there are some limitations associated with the current design. The slight discrepancy observed between the pressure oscillation obtained in silico (8-20 cmH_2O) and in vitro (11-17 cmH_2O) may be attributed to discretization errors associated with the meshing of the computational model. Additionally, the idealized first-order Windkessel model implemented in ANSYS may not represent complex second-order resistive losses that would arise in a physical system. The lung simulator utilizes a variable piston that moves under changes in the tidal volume, where both viscous and frictional losses could be present.

When compared to similar emergency ventilators designed for use in these settings, our device supports a longer oscillation period, which affords greater flexibility and

control of respiratory rate. Further investigation is required to understand the effect of less predictable respiratory patterns, such as coughing and wheezing, that might take place mid-respiratory cycle or early exhalation stage. Moreover, the ability of our proposed device to adapt and recover from such disturbances has yet to be studied. While the oscillator responds robustly when patient-triggered breaths are introduced, an important measure for patient comfort, we recognize that the inspiratory rise time of 0.7 seconds is long compared to the settings used in traditional pressure-controlled ventilation (0-0.4 seconds). This in turn could increase the work of breathing and cause patient-ventilator dyssynchrony.

In summary, this chapter introduced a low-cost, rapidly deployable emergency ventilator using a novel fluidic oscillator design. Clinically relevant values for PEEP, PIP, and oscillation period were achieved according to consensus guidelines for emergency use ventilators, with model input parameters taken from COVID-19 patient data. Additionally, the design facilitates precise, independent control of these variables guided by CFD and experimental studies. The oscillator responds robustly when patient-triggered breaths are introduced, which could afford greater patient comfort during the ventilation. Finally, the operational concept of the oscillator was validated by the prototype testing, and PEEP and PIP values between 11-17 cmH_2O were achieved. Further tuning of the prototype may be necessary to extend this range to the 8-23 cmH_2O range demonstrated by the simulation. Further research may also explore the full range of design parameters (e.g. FC, SC, and EC screw depth) that determine the oscillator's functional performance.

Chapter 3

"FenFit 2D" - A Program for Automated Fenestration Fitting

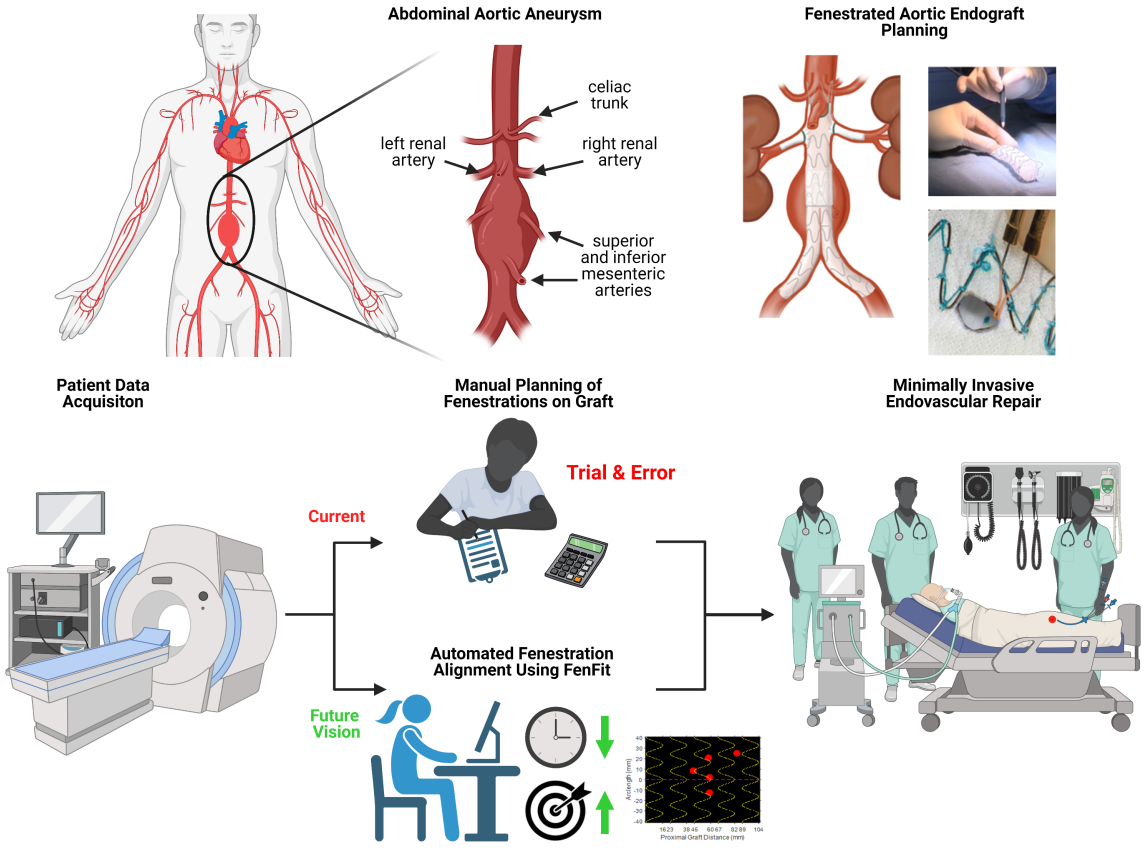

FenFit is an algorithm for automated alignment of fenestrations along juxtarenal endovascular grafts. This research was conducted in collaboration with Dr. Patric Liang Dr. Marc Schermerhorn at Beth Israel Deaconess Medical Center (BIDMC) / Harvard Medical School Teaching Hospital in Boston, Massachusetts. The purpose of this chapter is to highlight the approach taken to ideate, design, and deploy FenFit.

This chapter will begin with the problem statement and associated design requirements, before proposing a generalised workflow for improving treatment of AAA. Detailed design of the FenFit is discussed for both uniform and tapered graft scenarios. User Interface (UI) design considerations are highlighted also.

3.1 Introduction and Background

3.1.1 Condition and Treatment

The aorta is the largest artery in the body and carries oxygen-rich blood away from the left ventricle. An abdominal aortic aneurysm (AAA) is the dilation of the aortic diameter in all or a portion of the abdomen.

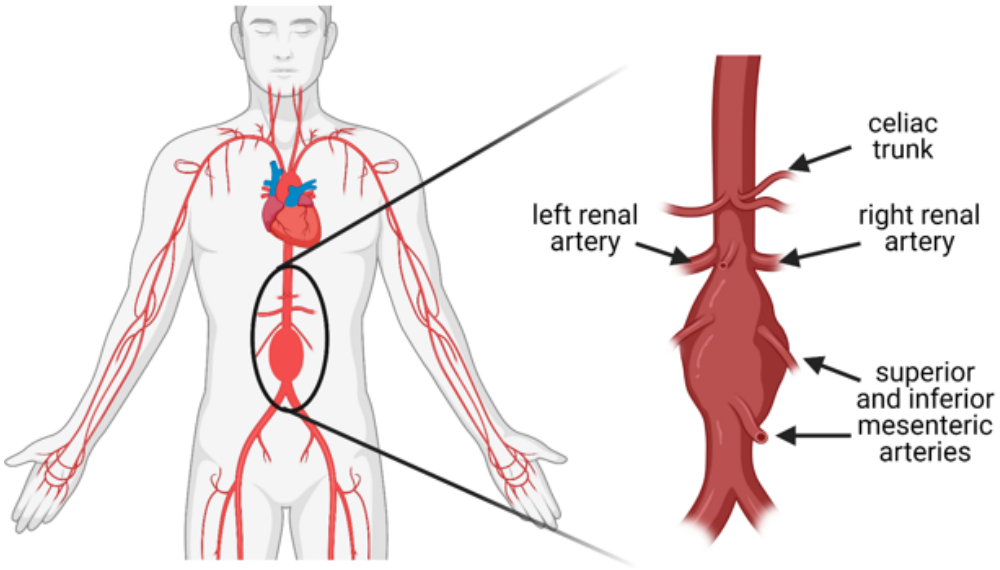

Figure 3-1: An Abdominal Aortic Aneurysm (created with Biorender^{TM}).

Risk factors for developing an aortic aneurysm include high blood pressure, atherosclerosis, genetic diseases that weaken connective tissue in the body (e.g. Marfan's syn-

drome and Ehler Danos syndrome), and traumatic injuries to the aorta (e.g. car accident) [4]. The incidence of AAA is 5-10 cases per 100,000 in the U.S. [45].

The primary treatment for this condition is to surgically implement an endovascular stent graft - a compliant tubular material reinforced with a metal stent mesh to mimic the biomechanics of the aortic wall. Two primary surgical techniques are used to implant aortic grafts inside the body - (1) open repair, and (2) endovascular repair (EVAR). During open repair, a large incision is made in the abdomen and the diseased tissue is replaced completely (Figure 3-2 A). This technique may be appropriate when the aneurysm is at a significantly high risk of rupture, though comes with the drawback of being quite invasive. A minimally invasive EVAR approach is often preferred by physicians, whereby a catheter is introduced through the femoral arteries, followed by an endograft which is unsheathed along the length of the catheter (Figure 3-2 B).

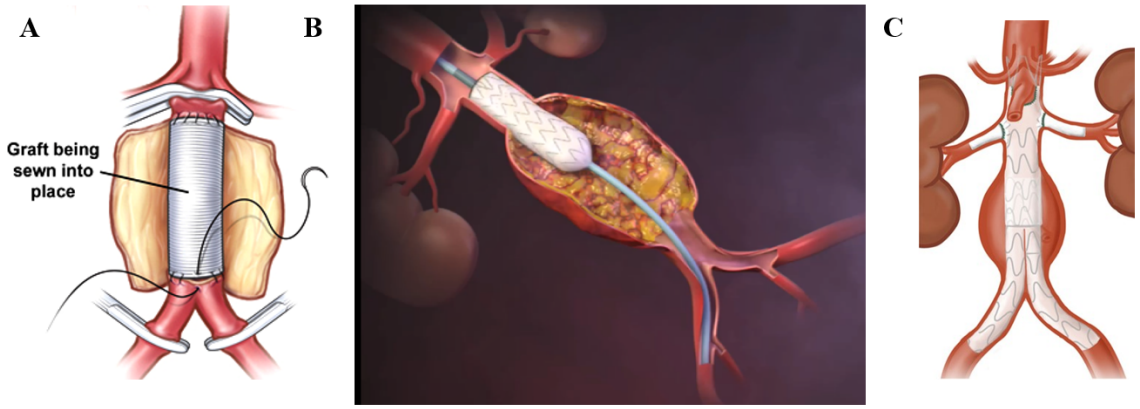

Figure 3-2: Open Aortic Surgical Repair (A), Minimally Invasive EVAR Deployment (B), Deployed Fenestrated EVAR graft (C) [28, 24, 46].

For aneurysms that extend across major abdominal vessels (i.e. juxtarenal aneurysms), a fenestrated endograft is required. A fenestration is a hole or sub-branch made in a graft to maintain blood flow (i.e. vessel patency) to various organs in the body. The presence of branches to the various arteries in the lower abdomen requires a patient-specific, fenestrated graft (Figure 3-2 C). This prevents chronic ischemia from lack of perfusion, reducing the risk of potentially fatal organ failure [2].

3.1.2 Problem Definition and Clinical Need

Given these designs are patient-specific and cannot be mass manufactured, several medical device companies (e.g. Medtronic and Abbott Laboratories) provide a service whereby the physician can provide an estimate of the fenestration locations, and the contractor will manufacture a hand-made, fenestrated graft. The lead time for this process can be in the order of a few weeks [6], which is often not feasible for a patient that presents with an urgent condition requiring immediate medical intervention. The service is also somewhat detached from the surgical planning procedure, in that there is little scope for the physician to fine-tune the design or preview the final product before it is shipped and manufactured.

To overcome this difficulty, vascular surgeons mostly choose to manually modify mass-manufactured, readily available, non-fenestrated grafts [52]. In doing so, physicians must account for the supporting stent structure, which maintains the structural integrity of the graft. The current state of the art graft planning workflow at BIDMC is as follows (also summarised in Figure 3-3):

1. Use CT imaging to determine the longitudinal and circumferential locations of each fenestration that may be obstructed by an EVAR graft in the aorta.

2. Use trial and error calculations to manually calculate orientations of the graft that maintain the patency of the fenestrations, while ensuring no overlap between the stent frame and fenestrations. This would require removal of a portion of the stent frame, which would compromise graft integrity.

3. Use a cautery pen (heat-conducting tool tip) to manually burn the fenestrations into a non-fenestrated endograft in the correct locations.

While there is some scope for improvement in the workflow of Steps 1 and 3, Step 2 tends to be the most tedious and is subject to calculation inaccuracies. For a particular graft orientation, there is no way of knowing *a priori* if the fenestrations will overlap the stent struts, mandating extensive trial and error on the physician's part.

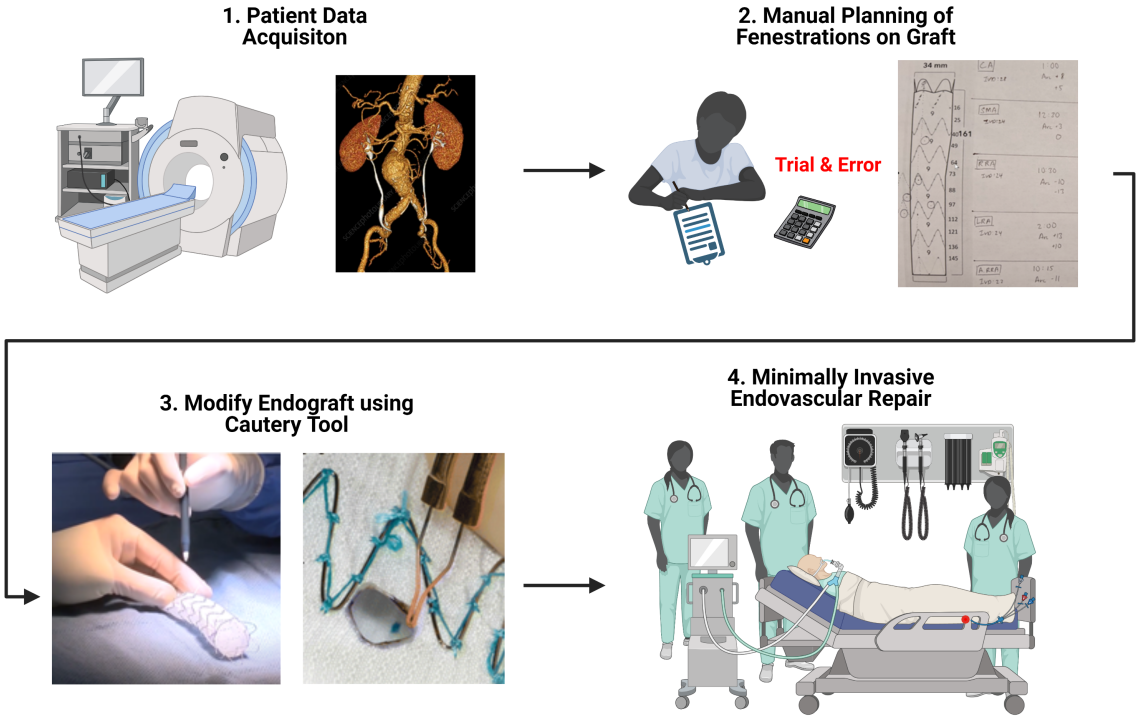

Figure 3-3: Current-state workflow utilized for physician-modified fenestrated EVAR planning procedures. CT data is segmented and used to determine the proximal and circumferential positions of each fenestration (1), the physician performs hand calculations to determine an alignment that ensures no alignment between the fenestrations and nearby stent struts (2), and a cautery tool is used to manually burn the correct fenestration locations in the graft (3), for use in minimally invasive EVAR surgery (4).

Based on the difficulties and limitations associated with the current workflow and outlined above, there appears to be a clear clinical need for improving the workflow involved in converting mass-manufactured grafts to patient-specific, fenestrated grafts, from both an efficiency and accuracy perspective.

3.1.3 Proposed Solution and Functional Requirements

The concept of a computer program was proposed as a means of tackling the accuracy and efficiency issues highlighted in section 3.1.2. This program will herein be referred to as FenFit. The following list highlights the initial functional requirements that were laid out for the program:

- Provide the physician with an intuitive, visual user interface for modifying endovascular grafts based on underlying patient-specific anatomy.
- Reduce the overall workflow time to perform the alignment process. Currently, the process takes approximately 1 hour at BIDMC.
- Allow the physician to modify any graft from a flexible design repository of both tapered and uniform diameter grafts.
- Provide a summary of the primary results in a standardised format, so that designs can be referenced and communicated amongst physicians.
- Render the modified graft selection in 3D for the physician, to increase confidence that the algorithm has completed its task accurately.

Based on the above specifications, a program workflow was proposed, as illustrated in the figure below.

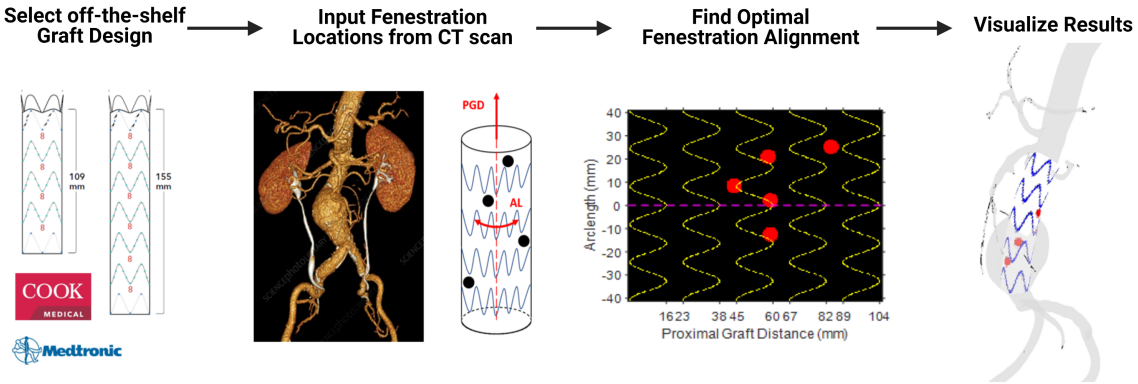

Figure 3-4: FenFit Automated Fenestration Alignment Program Workflow.

FenFit should first prompt the surgeon to input information from the patient's CT scan, and their preferred graft design. Following this FenFit will use MATLAB to search a viable design parameter space for the graft, given the constraints imposed by the patient's underlying anatomy. Finally, a graft design report should be compiled in a standardized format, facilitating communication and documentation amongst physicians. This format should mimic the preferred standard physicians are familiar with (in this case, BIDMC's template was used as a reference). Each component of this workflow will be discussed in turn in the following sections.

3.2 Algorithm Conceptual Design

FenFit was developed in MATLAB R2020b (The MathWorks, Inc., Waltham, MA, USA) given the extensive matrix manipulation and image processing techniques required for the program. MATLAB runtime is included in the FenFit installation package, which allows the user to execute the source code without the need for a MATLAB license or any prior experience with the program. The purpose of FenFit is to search a viable parameter space for the fenestrations on the graft, given the constraints imposed by both the patient's underlying anatomy and graft design.

From a computational standpoint, it is less expensive to conduct the alignment process on a flat 2D transformation of the graft's cylindrical 3D geometry. The fenestrations are projected from a 3D cylindrical co-ordinate system to a flattened 2D template, where the relative distance between fenestrations in the patient anatomy remains fixed. The computational challenge lies in determining an optimal longitudinal and rotational orientation for a given graft design (on the 2D template, this corresponds to movement in the arclength (AL) and proximal graft distance (PGD), as indicated in Figure 3-5).

To reduce computational expense, the graft space is divided into discrete parts, and the program searches over a finite number of fenestration placement configurations. The discrete step size is set to 1mm by default, though this parameter can be changed for finer placement resolution. MATLAB Image Processing Toolbox facilitates easy manipulation of these discrete components as pixels on a 2D image of the

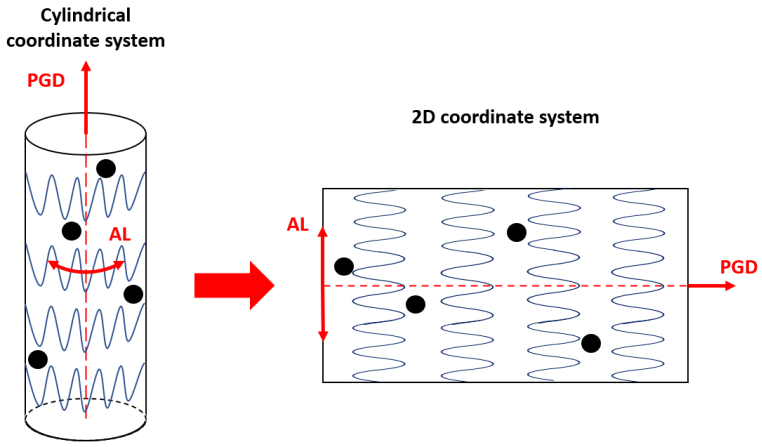

Figure 3-5: Transformation from 3D to 2D coordinate system to reduce computational expense in FenFit.

graft. From here, two image masks are generated: (1) a graft mask which determines the overall dimensions of the graft and stent struts, and (2) a fenestration mask, that defines the relative distances between the fenestrations. During the search process, the fenestration mask incrementally slides over the graft mask, and the program searches for overlap or collisions between the two, as depicted in Figure 3-6.

The details of mask generation and search methods will be discussed in more detail in the following sections.

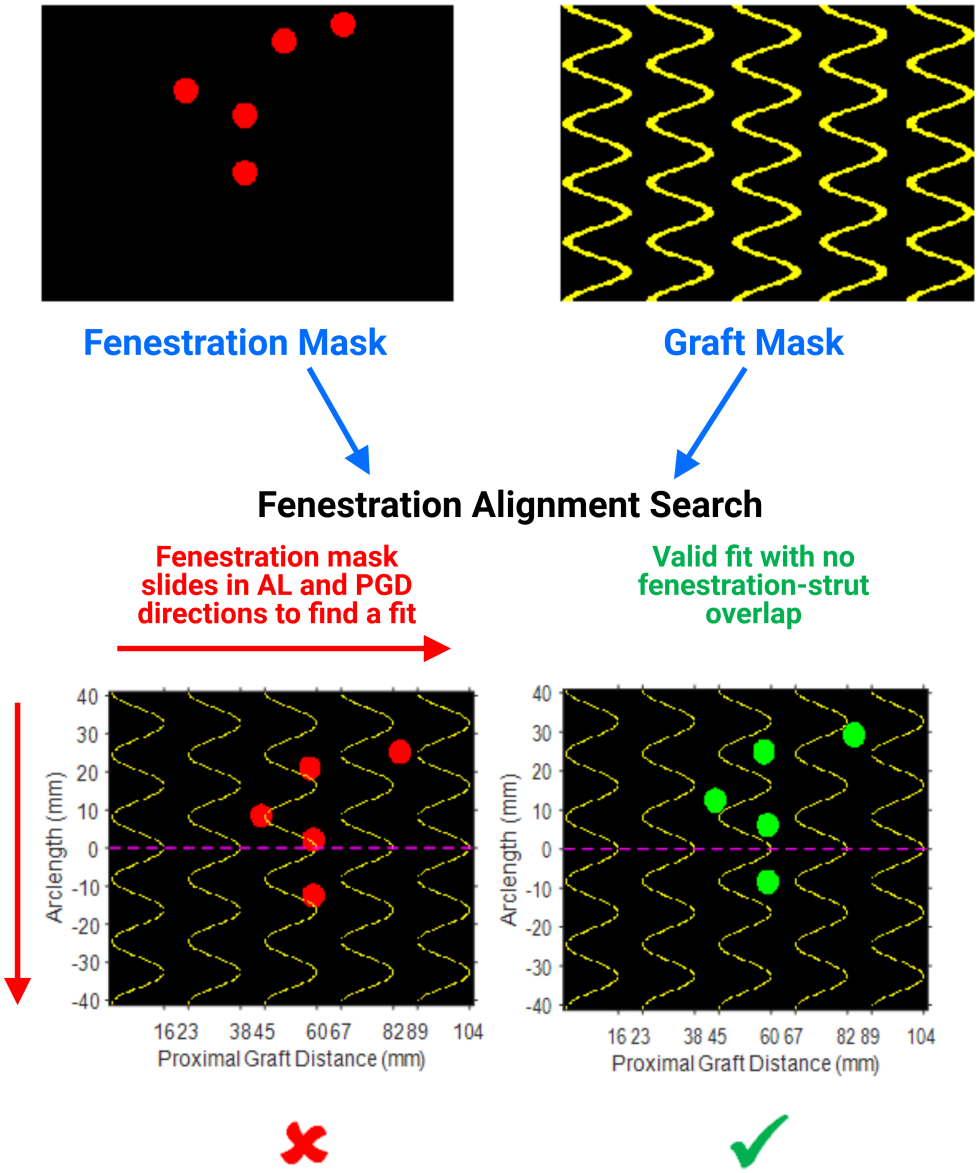

Figure 3-6: **FenFit search algorithm**. The fenestration mask based on patient anatomy and graft orientation (top left), and graft mask based on the physician's selected graft design are generated (top right). During the search, these masks are combined, and the algorithm searches for collisions to determine if a particular graft orientation provides a valid fit (bottom). FenFit continually slides the fenestration mask along the graft mask in the arclength (AL) and proximal graft distance (PGD) directions until all valid fits are located.

3.3 Algorithm Detailed Design and User Interface

3.3.1 Graft Selection

Both tapered and straight grafts can be used for FenFit. Cook Medical Alpha thoracic grafts [29] were used as the main repository for this study, as this is what our collaborators at BIDMC use for their procedures. It is worth noting that the program is flexible enough to include any number of databases or commercially-available graft designs, given appropriate information about their critical design parameters (e.g graft length, diameter, number of stent struts etc.).

As mentioned previously, spatially, there are an infinite number of locations the fenestrations could be aligned on the graft, and computationally, it is only feasible to divide the graft into a finite number of discrete parts. Depending on the memory capabilities of the computer being used, the user can select a particular resolution, or pixels per millimetre ($PPMM$) for the graft.

The design repository is inherently parametric, in that only a few key variables of the graft are necessary to introduce a new design in FenFit. The footprint of the flattened cylindrical graft is a rectangle of size $(\pi D) \times L$. Initially a binary mask template is generated, where '1' represents a pixel containing a strut, and '0' represents a free area of the graft where fenestrations can be placed. Based on the wavelength, λ, and amplitude, A, of the stent struts, a cosine wave can be generated for all N stent rings on the 2D template. A gap of GL spaces each cosine wave. All variables are scaled up by $PPMM$. This information is summarized in Figure 3-7. Also shown is the UI the user is prompted with when they first enter the program, where they may preview graft dimensions from the design repository on screen before moving onto the next step.

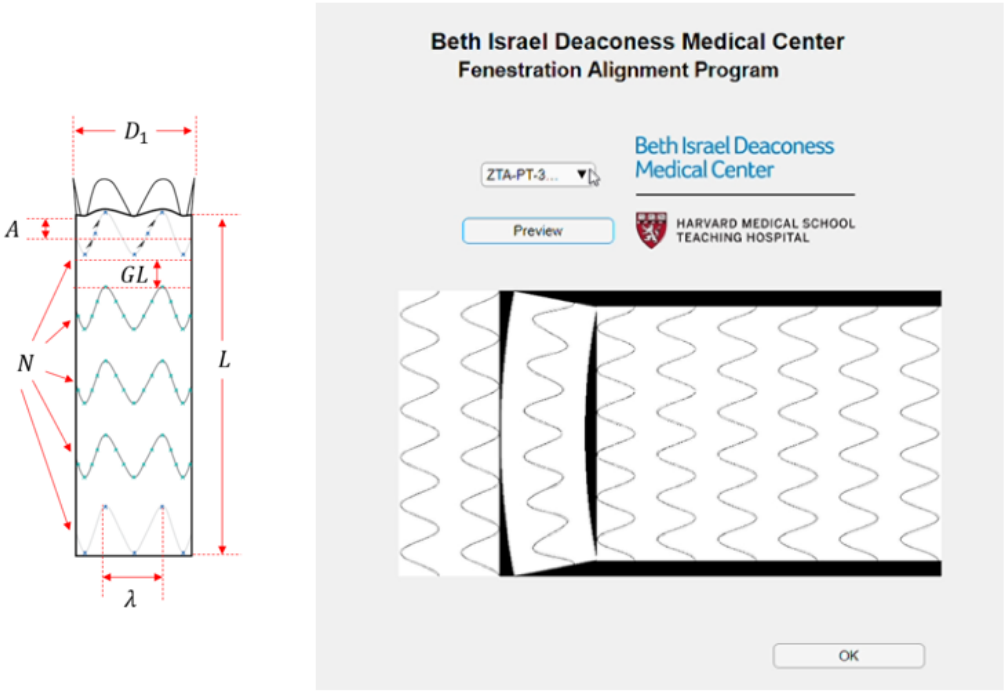

Figure 3-7: Critical graft design parameters (left) and previewing 2D graft template dimensions in the UI (right), where N is the number of stent struts, D is the graft diameter, GL is the gap length, A is the strut height, λ is the wavelength of the struts, and L is the overall graft length.

3.3.2 Inputting Patient Anatomy

After selecting a graft design, the next step in FenFit is for the surgeon to input information about the patient's anatomy. Cylindrical-planar mapping as highlighted in Figure 3-5 is utilized. Figure 3-8 demonstrates the second UI panel where the surgeon is prompted to input the AL, PGD and other measurements as obtained from the CT scan. Also included in the interface are instructions on how to use the cylindrical reference system for new users. The key variables the user must input are: the arclength (circumferential distance around the graft), the proximal graft distance, (distance from the fenestration to the top of the graft), the inner vessel diameter (or IVD, as measured at the level of the fenestration), and the fenestration diameter.

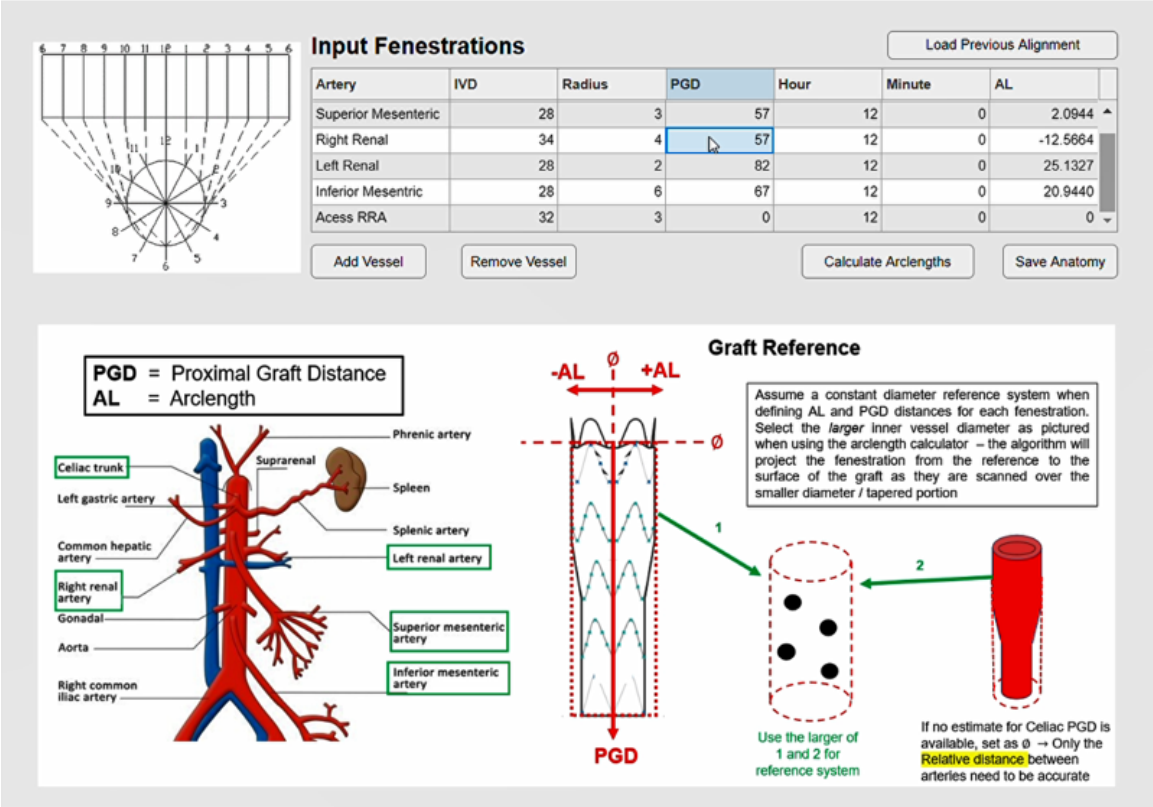

Figure 3-8: Input interface for visceral vessels to FenFit. Also included are instructions on the graft reference and coordinate systems utilized by the program.

The "clockface" convention is commonly used when measuring circumferential fenestration positions on axial slices of the the CT scan [52] (also the convention used at BIDMC). The angle left or right of a sagittal (12 o'clock) datum vector is used as a reference in estimating the clockface position of a given fenestration (illustrated in Figure 3-8). The user can choose to input AL values directly, or have FenFit calculate them automatically based on clockface measurements. For a given fenestration angle located in a cylindrical coordinate system, arclength is proportional to IVD, which is accounted for in the conversion.

Additionally, the user can modify the number of fenestrations to be included in the alignment and provide a label identifier for each of these. Finally, if the user is performing multiple program runs while testing variables incrementally, repetition is minimized by using the "Load Previous Alignment" and "Save Anatomy" options.

3.3.3 Search Algorithm Details

As mentioned in section 3.2, the fenestration holes cannot "collide" with the stent struts as it would not be possible to cauterize the fenestration holes through a metallic strut. One of the aims of the program, therefore, is to prevent collisions between the fenestration with the strut masks. After selecting a non-fenestrated graft design and providing visceral vessels to FenFit, the program conducts one or more of the following searches:

- **A favored search** – this is the first search conducted, which identifies configurations where there is no overlap between the stent struts and the visceral fenestrations.
- **A revised search** – this search is conducted only when a favored search fails, implementing posterior adjustment of the left and right renal arteries and 'non-priority' vessels, to increase the likelihood of finding a valid fit.

The favored search is conducted iteratively as follows:

1. A stent strut mask and fenestration mask are generated by setting all pixels within a radius of R of the fenestration center to a value of '1'. The strut mask can be produced by using simple parametric cosine equations that depend on the input parameters A, λ, and GL.
2. The fenestration mask incrementally slides over the fenestration mask in default 1mm increments (in both the AL and PGD directions, sequentially).
3. The program determines if each configuration is a valid fit; that is, that no collision has occurred between the two masks (Figure 3-6). To detect a collision, FenFit checks if any pixel value sums to '2' after adding the stent strut mask to the fenestration mask.
4. When a valid fit is found, a 'summed fenestration to stent strut distance' is calculated; a heuristic used to measure FenFit performance, defined as the collec-

tive distance between each fenestration and the nearest stent strut (highlighted in Figure 3-9).

5. Finally, when the search process is complete, all valid fits are rank-ordered based on summed distance.

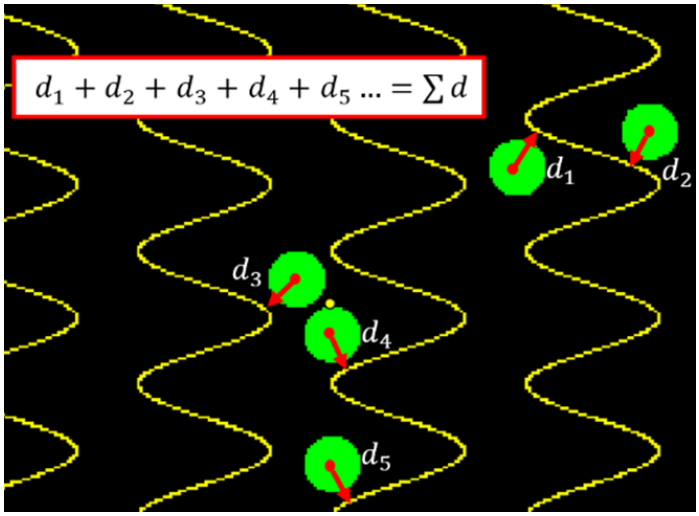

Figure 3-9: **Calculation of the 'Summed Distance' heuristic**; the combined distance between the centre of each fenestration and the edge of the most adjacent stent strut

.

In the event that the favored search locates no valid fits, the program conducts a revised search. In this mode, the fit for some vessels is prioritized over others.

During a revised search, the user can define 4 different vessel types: (1) a priority vessel, where no overlap is permitted between the fenestrations and the stent struts. (2) A non-priority vessel, where some overlap is allowed. (3) For the LRA and (4) RRA options, the left and right renal arteries may undergo up to 3mm posterior adjustment to achieve a valid fit. The degrees of freedom introduced via a revised search are highlighted in Figure 3-10, where the orange fenestrations may adjust independently of the prioritized vessels. The left and right renal fenestrations may undergo up to 3mm posterior adjustment each (movement in the circumferential direction towards the posterior side of the graft). FenFit will select the minimal posterior adjustment of the renal fenestrations that obtains an overall valid fit. The program also allows

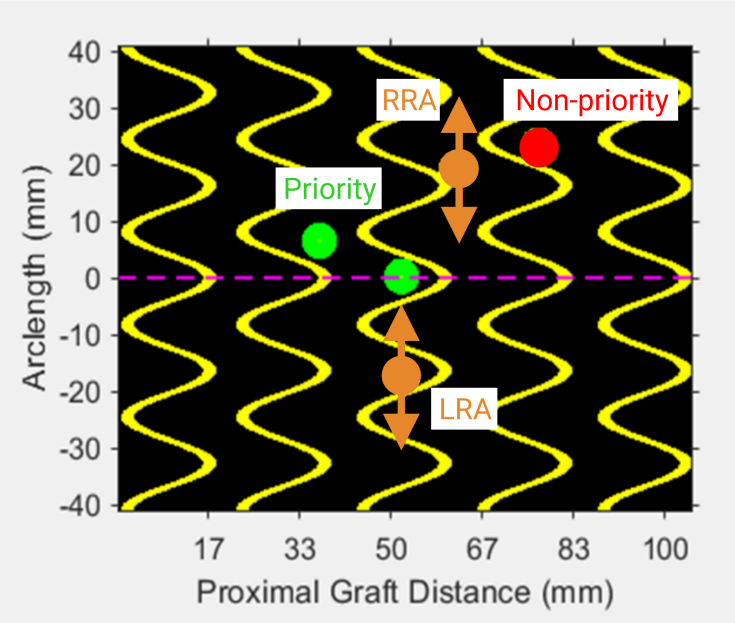

Figure 3-10: **Fenestration degrees of freedom under revised search regime**. For a given valid fit of the priority vessels, non-priority vessels may overlap the stent struts. Moreover, the LRA and RRA vessels may adjust in the AL directions.

the physician to manually adjust the patient geometry by clicking and dragging the fenestration after the best possible fit is determined. Finally, the user can cycle through all valid fits, rank ordered based on the summed distance.

3.3.4 Tapered Geometry Considerations

Tapered EVAR may be required in certain portions of the aorta that see an abrupt change cross section in the distal direction [31]. While the basic search functionality of the program is the same for tapered grafts as that described in the previous sections, the 3D to 2D mapping transformation differs when considering simultaneous movement of the fenestrations. The uniform proximal and distal portions of the graft are mapped as separate uniform diameter grafts, where scaling is applied to account for their varying diameters. The tapered portion of the graft can be viewed as a truncated cone geometry (i.e. a frustrum), which maps to a truncated circle sector in 2D. The 2D coordinate system, therefore, can be split into 3 discrete portions for implementation in FenFit (depicted in Figure 3-11).

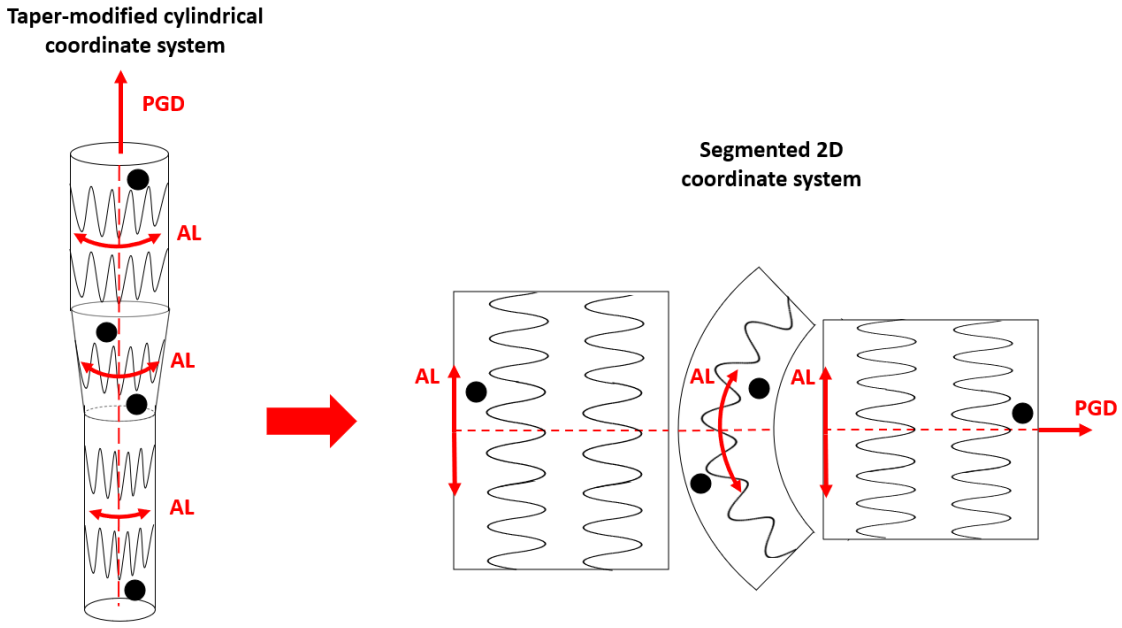

Figure 3-11: Transformation from tapered 3D coordinate system to segmented 2D coordinate system in FenFit. The red arrows indicate movement of the fenestrations in each coordinate system.

Under rotational and longitudinal movement of the graft, the fenestrations will move along the AL and PGD directions in different ways depending on the portion of the graft in which they are located. On the larger diameter proximal portion of the graft, the fenestrations will move further in the AL direction for a given rotation

angle than the distal portion of the graft. A scaling factor k, defined by $\frac{D_2}{D_1}$, was implemented to account for this.

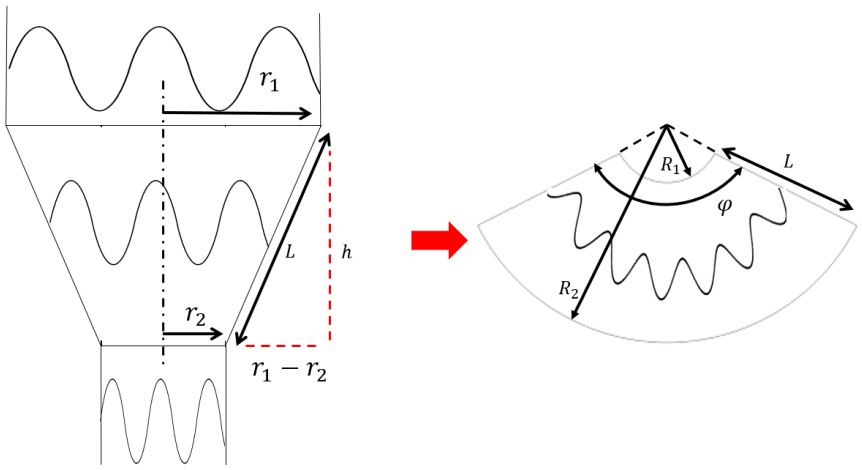

Figure 3-12: Calculation of truncated sector dimensions for 2D mapping of the tapered graft portion.

For the tapered portion, fenestrations no longer move in parallel directions as the graft is moved rotationally and axially. The dimensions of the truncated sector can be determined using trigonometry based on the graft parameters in Figure 3-12:

$$L = \sqrt{(r_2 - r_1)^2 + h^2} \tag{3.1}$$

$$R_1 = \frac{Lr_1}{r_1 - r_2} \tag{3.2}$$

$$R_2 = L + R_1 \tag{3.3}$$

$$\phi = 360 * \frac{r_2}{R_2} \tag{3.4}$$

Where r_1 and r_2 are the large and small diameters of the graft respectively, and h is the vertical length of the tapered portion as indicated in Figure 3-12. After calculating the variables in 3.4, a binary image mask can be generated for the tapered cosine wave,

$$fen_x(t) = C_x + \left[(R_{base} + A)\cos\frac{2\pi nt}{\phi}\right]\cos t \tag{3.5}$$

$$fen_y(t) = C_y + \left[(R_{base} + A)\cos\frac{2\pi nt}{\phi}\right]\sin t \tag{3.6}$$

Where C is the center of curvature, R_{base} is the zero-amplitude reference of the strut interpolated between R_1 and R_2, and n is the number of struts per circumference. Note the product of cosines in the equation above provides a parametric representation of a cosine wave over a circular arc. Therefore, movement of the fenestrations in the arclength direction is curved on the tapered portion of the graft. The Euclidean PGD-AL axes on the uniform diameter coordinate system become polar r-θ axes on the tapered portion. The tapered fenestrations will move in an arc $(C_x + r\cos\theta, C_y + r\sin\theta)$ under rotation of the graft. Conditional statements are necessary to vary the mapping transformation depending on the PGD of each fenestration (i.e. the larger diameter (1), tapered (2), or smaller diameter (3)). This concept is highlighted in Figure 3-13.

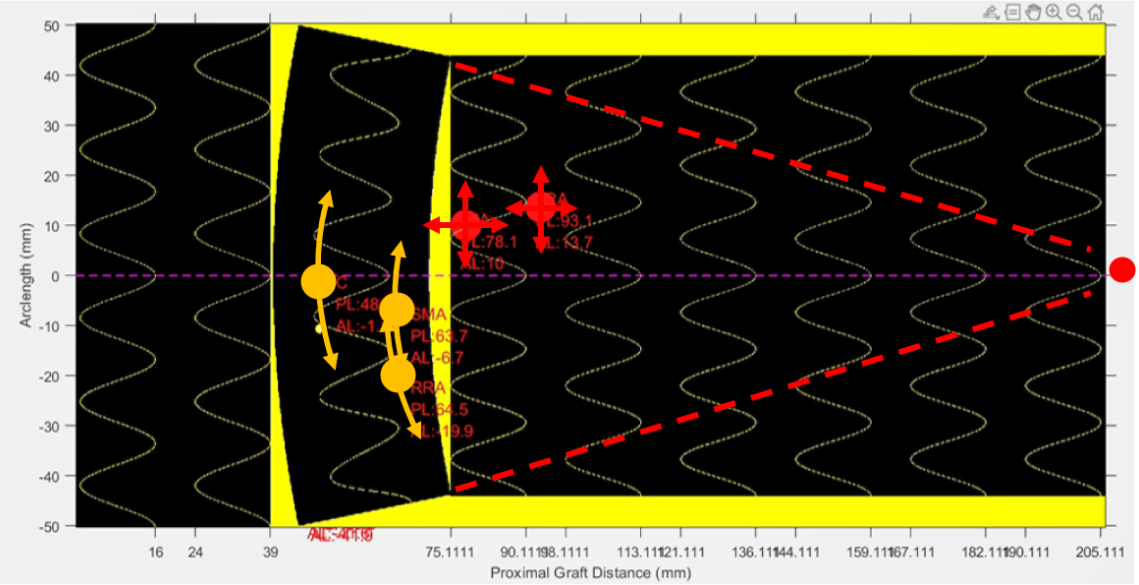

Figure 3-13: 2D fenestration movement for a tapered graft. On the tapered portion of the graft, the fenestrations move in an arc (orange).

3.3.5 Report Generation

When the user is content with their alignment selection, the final step is to render the fitted graft on screen and generate a report. FenFit fills "holes" in a word document template automatically based on the user's final selected alignment. This document was formatted based on BIDMC's desired standard, and can be modified to suit the preferences of other hospitals / physicians. An example of this report is shown in Figure 3-14.

Beth Israel Deaconess Medical Center

HARVARD MEDICAL SCHOOL TEACHING HOSPITAL

GraftAlign Report

PGD = Proximal Graft Distance; AL = Arclength; IVD = Inner Vessel Diameter (all in mm)

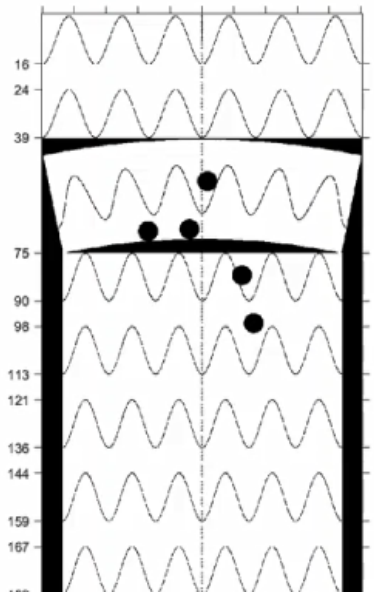

Artery	IVD	Hours	Mins	AL	PGD	Notes
Celiac	32	12	11	1.6	52.7	
Superior Mesenteric	28	11	28	-4.1	67.7	
Right Renal	28	9	45	-17	68.4	
Left Renal	28	2	8	16.2	97.1	
Inferior Mesentric	28	1	39	12.5	82.1	

Figure 3-14: **Example of FenFit auto-generated report**. This report was generated based on BIDMC's standard formatting.

3.4 Clinical Trial Testing

To test the efficacy of FenFit in producing a valid graft alignment that is both accurate and efficiently obtained, a set of clincial trials were conducted by our clinical collaborators at BIDMC, Boston. All consecutive patients scheduled to undergo fenestrated aortic endovascular repair of juxtarenal aortic aneurysms at BIDMC from January 2017 to January 2021. Cases use to compare planning results between FenFit and the physician were limited to those after the development of the program in September 2020. Preoperative CT images were initially reviewed for treatment candidacy using the ConserusTM Enterprise Viewing System (Change Healthcare, Nashville, TN), and the determination that the patient was high risk for open aortic surgery and would be treated using a custom-fenestrated device was determined by the treating physician. Centerline reconstruction and patient anatomical parameters including AL and PGD measurements were obtained using TeraRecon software (TeraRecon, Inc., Durham, NC). These aortic fenestration measurements were then inputted into the FenFit program for automated alignment. This study was approved by the Beth Israel Deaconess Institutional Review Board and gave permission to use imaging data without the need for individual patient informed consent due to the de-identified nature of the data.

Optimal patient-specific visceral fenestration positioning on a Cook Medical Alpha thoracic endograft was determined independently by the physician and FenFit. The primary outcome was best visceral fenestration fit positioning on a Cook Medical Alpha thoracic endograft, quantitively assessed by the summed fenestration to stent strut clearance distance as described previously, as well as the speed at which a fenestration fit was located. Fenestration planning time was measured for the time elapsed for the program or physician to find a valid fit after obtaining the relative orientation of the visceral fenestrations based on TeraRecon centerline reconstruction. 3 vascular surgery physicians were randomly assigned to each of the clinical cases, performed the calculations, and found the visceral fits independently.

Of the 118 total physician modified endograft cases identified, FenFit was utilized in 25 of the cases. Of these FenFit cases, 14 (56%) were planned using a tapered grafts, and 11 (44%) using a straight grafts, using 3 to 5 visceral fenestrations. Fenestration fit without the need for posterior renal artery fenestration adjustment (as described in section 3.3.3) was achieved in only 12 cases (48%). The fenestration alignment program resulted in a significantly shorter fenestration planning time compared with surgeon planning (median 0.6 min [IQR 0.4-1.5min] vs. 23.0 min [17.1-26.2min], P $<$ .001). Although the FenFit alignment program confirmed an identical or similar fenestration fit as the physician plan in 13 cases (52%), the program identified an improved fenestration fit in 7 cases (28%), defined by an averaged summed fenestration to strut clearance distance increase of 5.6±3.6mm. Additionally, FenFit identified 5 cases (20%) where the physician plan failed to achieve a fit (n=3), or determined that posterior renal fenestration adjustment was unnecessary to achieve a fit (n=2).

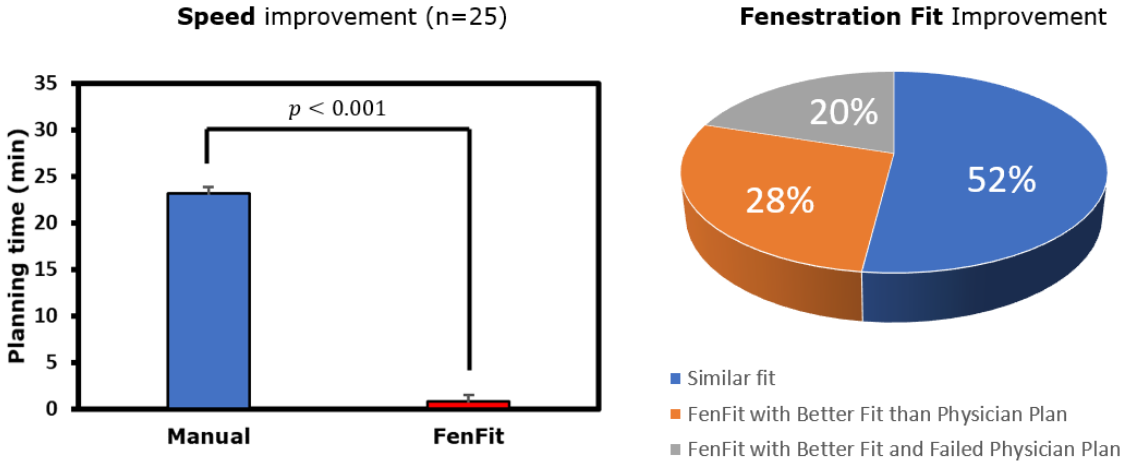

Figure 3-15: **Summary of FenFit retrospective clinical trial results**. Comparison of FenFit and physician manual case planning time (left). Improvement in accuracy offered by FenFit over physician manual planning (right). p<0.05 was considered statistically significant.

Chapter 4

"FenFit 3D" - Fenestrated Graft Visualization

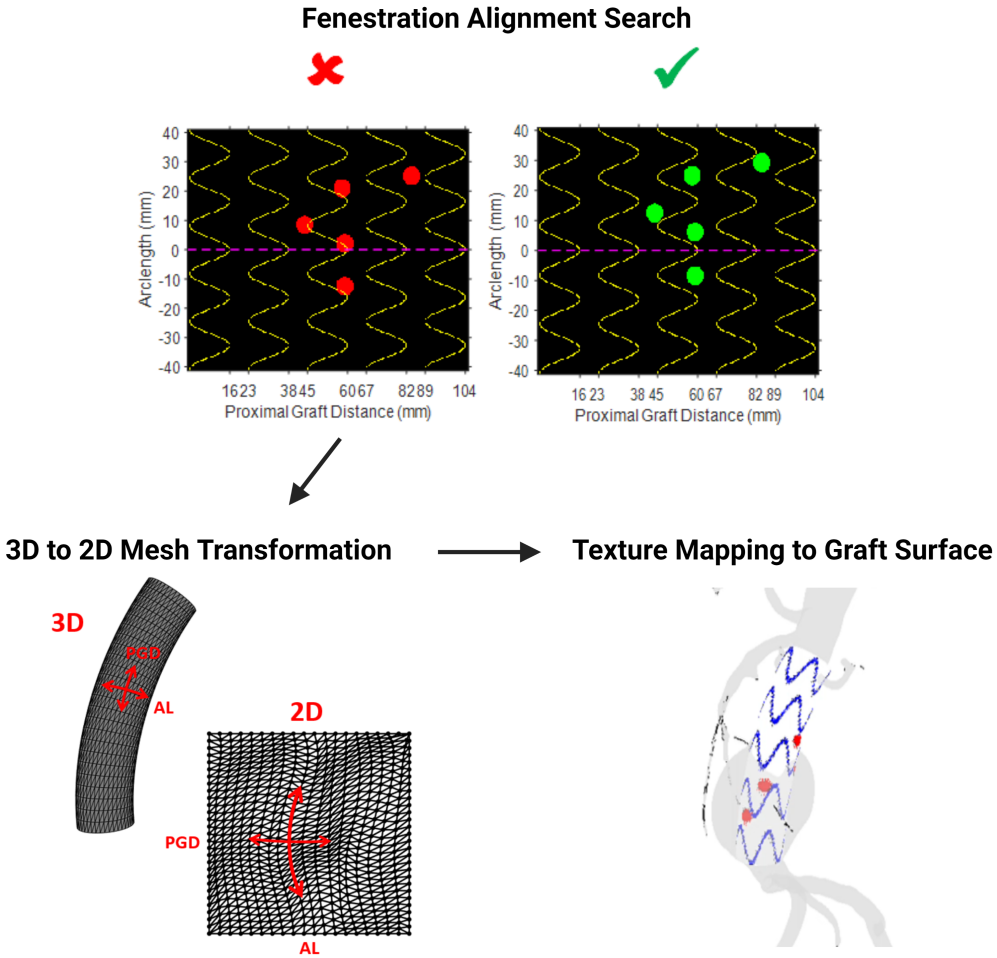

Chapter 3 described the methods utilized for automated fenestration fitting within FenFit. As previously mentioned, a key functional requirement of the FenFit involves 3D visualization of the final fenestrated graft design inside the aorta (Figure 3-4). This functionality would allow the physician to compare the graft design produced by FenFit against the initial segmented aortic anatomy. Though they are not critical in obtaining design instructions for the OR, extended visualization capabilities offer the following advantages over a 2D printout alone:

1. **Workflow transparency** - the user can generate a more intuitive spatial understanding of the 2D templates presented in Chapter 3, and how they relate to the patient's aortic anatomy.

2. **Algorithm Confidence** - As with any novel surgical technology, there will always be some resistance from clinicians who prefer traditional techniques. Visualization capabilities may allow such physicians to gain trust in the efficacy of FenFit to produce a valid fenestrated graft design, which should translate to faster, more widespread adoption of the program.

3. **Intra-operative and Post-operative Comparison** - 3D visualization offers an ideal graft configuration to aim for during FEVAR deployment, as well as a baseline for clinicians to verify the postoperative integrity of the graft.

Given the clear advantages outlined above, an algorithm for graft visualization was proposed. This algorithm provides a more generalized method for generating 2D texture maps of the deformed 3D graft, which will substitute for the less flexible parametric transformation maps presented in Chapter 3.

The overall algorithmic approach utilized in the 3D visualization component of FenFit is highlighted in Figure 4-1. The algorithm can be applied to all non-manifold graft geometries, facilitating flexibility to introduce more diverse graft designs in future (e.g. bifurcations, graft branching etc.).

The open source tool 3D Slicer [35] was used to segment and extract the aortic anatomies for this study. In practice, any medical imaging software with segmentation

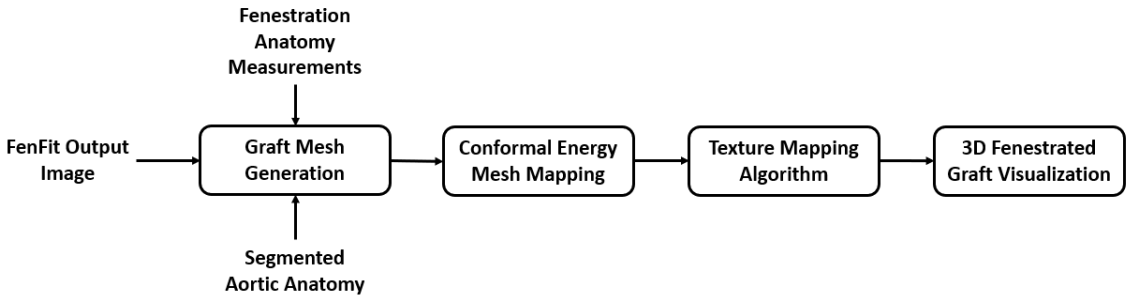

Figure 4-1: 3D visualization algorithm to be described in Chapter 4.

capabilities could be used for this process. In chapter 5, potential future work is highlighted related to integration of FenFit with segmentation programs for automatic aortic segmentation and extraction of the relevant visceral anatomy measurements.

GIBBON [32] is an open-source MATLAB toolbox that includes an array of image and geometry visualization and processing tools, and was used to develop most of the geometry manipulation functions highlighted in the following sections.

In the following sections, development and testing of the functions highlighted in Figure 4-1 are described in detail. Experimentation of the overall workflow with real AAA patient data is also presented.

4.1 Graft Mesh Generation

Before introduction of the patient anatomy to FenFit, pre-processing of the aortic CT scan is required. Most CT imaging programs are capable of automatically segmenting the aortic anatomy for creation of a 3D model (e.g. Slicer, Terarecon or similar [35]). These programs use machine learning algorithms to generate a tree of interconnected 3D nodes based on the Hounsfield Unit (HU), a measure of radio-intensity used in CT imaging. The aorta can be isolated using this method, given the HU of blood can usually be distinguished from the surrounding tissues. Some segmentation programs may also have capabilities to automatically extract the aortic centreline using machine learning algorithms and centroid cross section calculations [12]. Potential future work may examine automated segmentation and extraction of the relevant visceral anatomy to be made compatible with FenFit, so that all functionality can be contained within

one program (see Chapter 5 for more details).

The first component of FenFit's visualization algorithm is to generate a 3D cylindrical graft mesh suitable for texture mapping. To describe the approach employed at a high level, graft normals were first calculated based on CT aortic centerline data for generation of a cubic spline. A circular profile was then swept along the spline to obtain the final cylindrical graft mesh.

To obtain the most realistic simulation of the graft inside the aorta, it is useful to assume that its deployed shape will not violate the graft's bending mechanics. Assuming the graft shape can be approximated as a uniform continuous beam under bending, the Euler-Bernoulli equation applies as follows,

$$EI\frac{d^4u}{dx^4} = q(x) \tag{4.1}$$

Where $k = EI$ is the graft bending stiffness, u is deflection and q is the applied transverse load. Physically, splines come from bending a long thin beam to give it the correct deflections at defined interpolation points [34]. A smoothing spline f is defined as the curve that minimizes the optimization function,

$$\sum (U_i - \hat{f}(x))^2 + \lambda \int f''(x)^2 dx \tag{4.2}$$

Where U are the coordinates of the aortic centerline, $\hat{f}$ is the smoothing spline, and λ is the second derivative roughness measure. Note that as λ goes to infinity in the equation above, the spline approaches a linear least squares optimization. To minimize noise in the data set, the centerline ends were selected as interpolation points, and the profile normals at the top and bottom of the graft were defined to constrain the spline's slope. The graft is then free to choose its own shape under the solution to $\frac{d^4u}{dx^4} = 0$, which in this case is an ordinary cubic spline. This result aligns with the solution we would expect from equation 4.1.

To determine the direction of the endpoint profile normals at the top and bottom of the graft, Singular Value Decomposition (SVD) was applied to the first 10% and last 10% of points along the aortic centerline. SVD is a generalization of eigendecomposition for non-square matrices [49]. For this application, we wish to determine a 3D line of best fit to obtain the x, y, and z components of the normal vectors. An m x n matrix can be factorized into a product of 3 matrices under SVD as follows:

$$X = U\Sigma V^T \tag{4.3}$$

Where X is the data matrix that is factorized to a left singular matrix U, the diagonal matrix Σ of singular values, and the right singular matrix V. The columns of the matrix U represent the orthonormal basis vectors (or principal components) of the data matrix X. The columns associated with the largest singular values describe most of the variance in X (those closer to the left). As such, U can provide an approximation for X, whose accuracy depends on the number of truncated columns. In this case, the first column vector in U is the 3D line of best fit that describes the graft normals. Sample results obtained through application of equations 4.2 and 4.3 are illustrated in Figure 4-2.

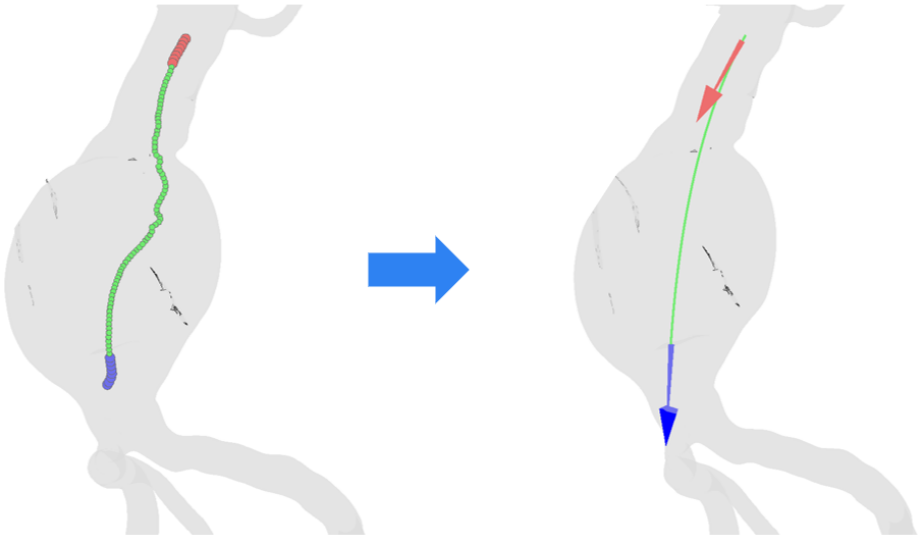

Figure 4-2: Graft endpoint normals for a noisy aortic centerline generated using the SVD approach, and corresponding cubic spline of best fit (highlighted in green).

A graft profile must be defined that will be swept through the best fit cubic spline. A function was developed that takes the user's graft diameter selection as an input, and outputs a base and top graft profile appropriate for sweeping. These profiles lie on a plane perpendicular to the centerline normals, n as depicted in Figure 4-3. During conventional fenestration planning, AL measurements are measured relative to the sagittal plane direction [52]. The mesh nodal directions should be aligned with the AL and PGD axes to account for this, such that the final FenFit output maps to the correct rotational orientation on the 3D graft.

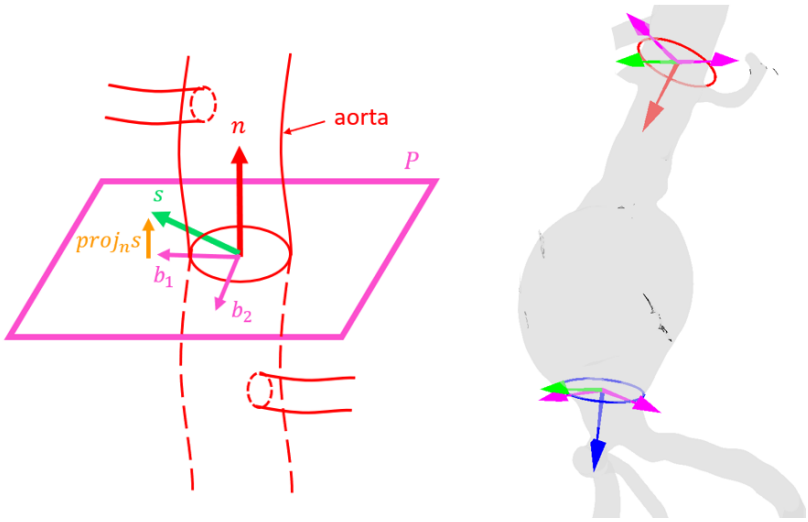

Figure 4-3: Calculation of the basis vectors b_1 and b_2 that define the plane P normal to the centerline vector n. b_1 is the vector rejection of the sagittal vector s on n.

The sagittal basis vector, s, is projected onto the top and bottom profile plane to act as the "12 o'clock" reference basis vector, ensuring a uniform AL reference system is used along the length of the graft. This vector is the orthogonal projection of s on n (also known as the vector rejection) and is calculated by,

$$b_1 = s - proj_s n = s - \frac{s \cdot n}{n \cdot n} n \tag{4.4}$$

Where b_1 is the first basis vector on the profile plane. The other basis vector, b_2, is calculated via the cross product of n and b_1. The graft profile is then generated by rotating a circular cross section through b_1 and b_2.

Finally, a lofting function from the GIBBON toolbox [32] was used to sweep a surface mesh along the previously determined spline of best fit, which uses the Kabsch algorithm [21] as follows,

1. **Initial Sweep Estimate** - all points on the top profile are swept parallel to the cubic spline to determine an initial estimate for the mesh vertex positions.

2. **Comparison of Actual Base Profile with Estimate** - A covariance matrix is calculated which provides a measure of the difference between the actual base profile, V_b (found using the method highlighted in Figure 4-3), and the base profile estimate determined via a parallel sweep, $\hat{V}_b$. The covariance matrix is represented by,

$$H = \hat{V}_b^T V_b \tag{4.5}$$

   Where V_b and $\hat{V}_b$ are both $nx3$ matrices of profile coordinates in 3D space.

3. **Calculation of Optimal Rotation Matrix** - The Kabsch algorithm determines an optimal rotation matrix by minimizing the root mean squared deviation between V_b and $\hat{V}_b$. SVD is applied to the matrix H, and the optimal rotation matrix R can be calculated from the left and right singular vectors [21],

$$R = VU^T \tag{4.6}$$

4. **Revised Sweep using Interpolated Rotation Matrix** - A modified parallel sweep of the top profile is performed, where R is scaled as a function of sweep depth and and applied to each cross section to ensure better alignment of V_b with $\hat{V}_b$ at the graft base.

Final results obtained via the graft mesh generation algorithm are shown in Figure 4-4 for both a uniform and tapered graft.

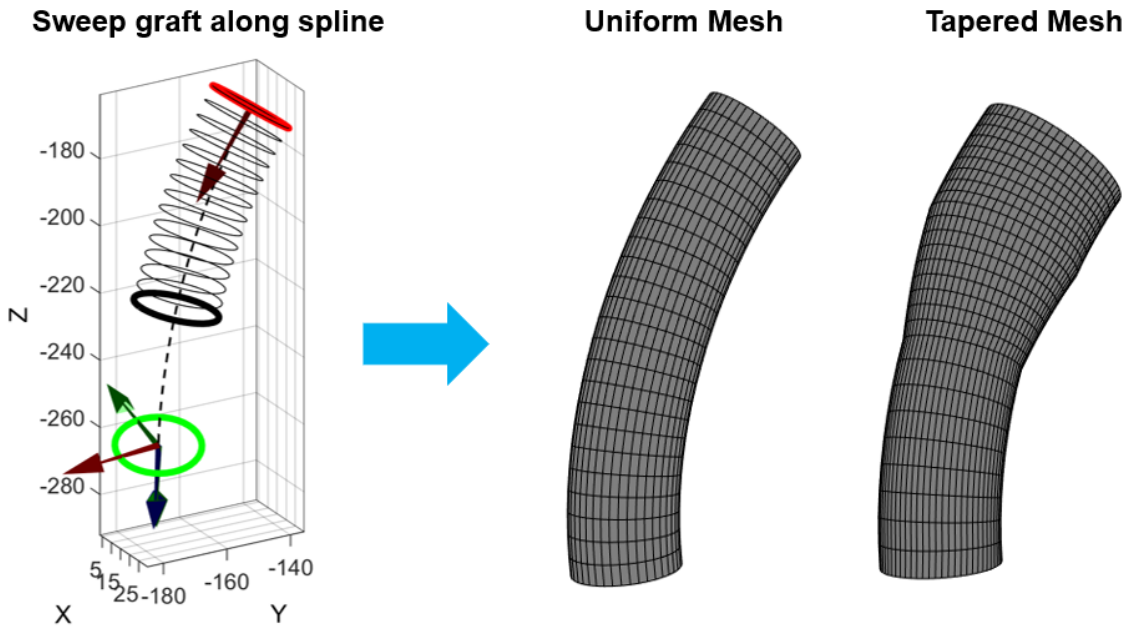

Figure 4-4: Sweeping graft mesh along best-fit spline using the Kabsch algorithm (left). Comparison of uniform and tapered graft mesh sweeps for the same aortic centreline (right).

4.2 2D Mesh Parameterization

In section 4.1, a 3D deformed graft mesh was generated based on the patient's visceral anatomy. To render a FenFit output image on the surface of this mesh, a bijective mapping function (or mesh parameterization) is required between the PGD-AL space and the deformed graft surface in $x-y-z$. The following section will outline methods used to obtain a deformed 2D representation of the curved graft mesh for 1-1 mapping of each vertex between the two domains.

There are many examples of dimensionality reduction algorithms and mesh flattening techniques capable of producing 2D representations of 3D topologies. Surface mapping algorithms have recently been applied to a number of applications in medical image processing. For example, Karim et al. [23] applied a surface flattening function to segmented models of the human left atrium for clinical applications. Hundal et al. [17] applied conformal mapping techniques to obtain planar representations of CT scans of the cerebral cortex. For this application, we require a transformation

that captures the connectivity, spacing, and angles between the mesh vertices for a valid representation of the 3D graft. One of the more methods found in the literature relates to spectral mesh flattening [51]. These techniques use a set of optimization functions to find 2D mesh locations that minimize the distortional "energy" under a mapping transformation (Levy [27] and Desbrun [9]). The principal eigenvalues of the mesh are often extracted to obtain the required dimensionality reduction [49]. However, this mesh parameterization is not always guaranteed to be bijective.

Given graft meshes are almost always smooth manifold geometries, a simpler, discrete laplacian mesh approach was found to be more suitable. The discrete laplacian matrix describes the degree (connectivity), and adjacency (distance) between vertices on a discrete grid [43],

$$L = D - W \tag{4.7}$$

Where L is the Laplacian matrix, D is the degree matrix, and W is the adjacency matrix. D is a diagonal matrix, which is m x m in size, where m is the number of vertices in the domain. This matrix represents the number of nearby vertices any given vertex is connected to. W is also an m x m matrix, where a non-zero off-diagonal term (i, j) represents a connection between the vertices i and j via an edge. Therefore, for meshes where m is particularly large, this matrix W is mostly sparse.

$$D = \begin{bmatrix} 2 & 0 & 0 & 0 \\ 0 & 3 & 0 & 0 \\ 0 & 0 & 3 & 0 \\ 0 & 0 & 0 & 2 \end{bmatrix} \qquad W = \begin{bmatrix} 0 & 1 & 1 & 0 \\ 1 & 0 & 1 & 1 \\ 1 & 1 & 0 & 1 \\ 0 & 1 & 1 & 0 \end{bmatrix}$$

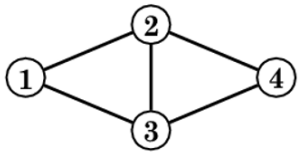

$$L = \begin{bmatrix} 2 & -1 & -1 & 0 \\ -1 & 3 & -1 & -1 \\ -1 & -1 & 3 & -1 \\ 0 & -1 & -1 & 2 \end{bmatrix}$$

Figure 4-5: Illustration of sample Discrete Graph Laplacian and corresponding degree and adjacency matrix for 4 interconnected vertices [41].

Equation 4.7 above retains information about connectivity and spacing under a 3D to 2D mapping transformation, though the operation is not necessarily angle

preserving (i.e. conformal). To refine the Laplacian matrix for this application, the canonical cotangent-weight Laplacian matrix was implemented. First proposed by Pinkall and Polthier [36], cotangent weights provide an indication of the weighted sum of all edge lengths and angles adjacent to vertex (as illustrated by Figure 4-6).

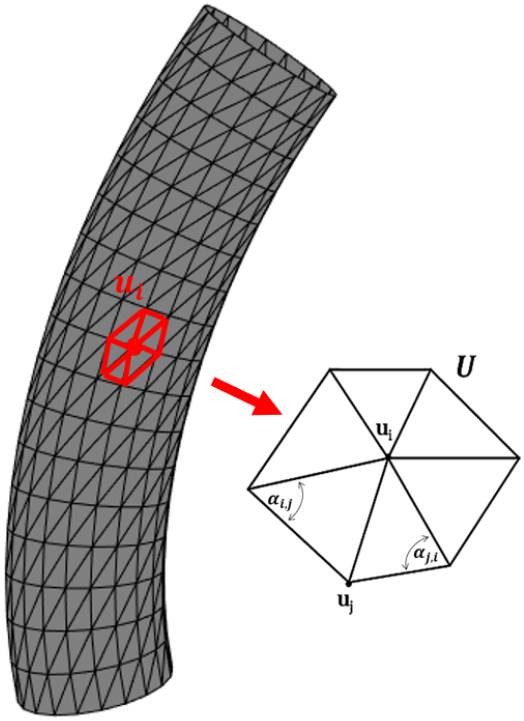

Figure 4-6: Relevant geometry for calculating cotangent weights at given vertex i.

The weights are calculated by,

$$L_{ij} = \begin{cases} w_{ij} = \frac{1}{2}(\cot \alpha_{ij} + \cot \beta_{ij}) & \text{if (i, j) is an edge} \\ w_{sum} = -\sum_{k \in N_i} w_{ik} & \text{for i=j} \\ w_{ij} = 0 & \text{otherwise} \end{cases}$$

Note in the formulae above that the terms w_{ij} correspond to a weighted variant of the previously described *adjacency* matrix, and the terms w_{sum} represent a weighted *degree* matrix. Together these terms combine to yield the discrete weighted Laplacian in a similar form to Equation 4.7. It is worth noting that cotangent weights also preserve angles (and consequently areas) more accurately than the standard Laplacian

matrix during reconstruction, providing a smoother overall appearance of the mesh (Figure 4-7).

During FEVAR planning, surgeons are most accustomed to interacting with a rectangular view of the PGD-AL axes. In utilizing the methods above alone, the deformed mesh boundary will not be constrained to any particular shape. Moreover, the rectangular FenFit output image will conform better to a rectangular boundary mesh, which in turn yields results under 3D texture mapping interpolation (section 4.3). Therefore, rectangular Neumann boundary conditions (BCs) (i.e. derivative-based BCs) were applied to the Laplacian mesh to constrain its shape. Similar to Neumann BCs implemented in computational fluid mechanics and other fields of finite element modeling, these BCs enforce no "flow" of the mesh outside the predefined boundaries [43].

A sample 3D graft mesh, its transformation under the discrete Laplacian transformation, and the same mesh constrained using Neumann boundary conditions are highlighted in the figure below.

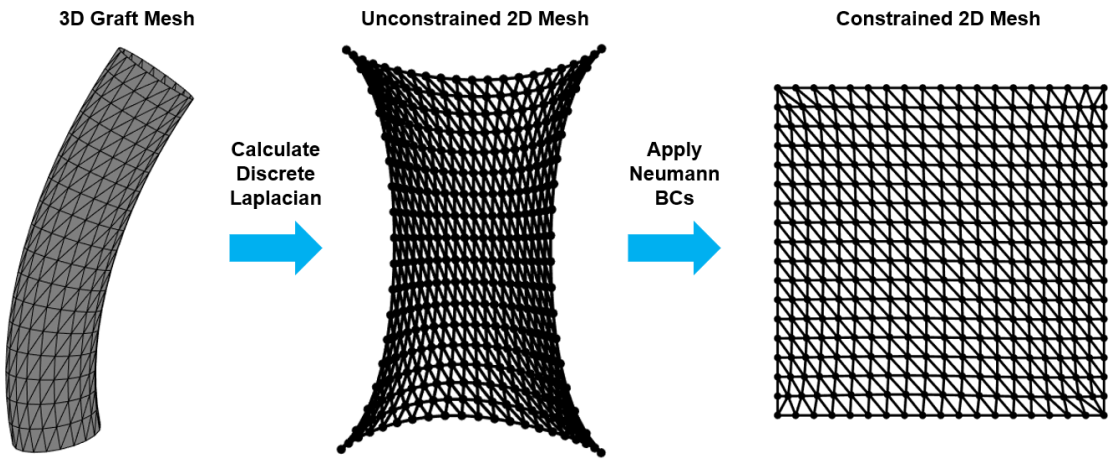

Figure 4-7: **Generation of a bijective 3D to 2D vertex mapping for a uniform graft**. The discrete laplacian matrix is calculated to determine the 2D degree and adjacency of the 3D graft vertices. The 2D mesh is then constrained to a triangle using Neumann boundary conditions (BCs) for enhanced conformal mapping of the FenFit output image.

4.3 Texture Mapping Algorithm

The final step of the 3D visualization algorithm involves texture mapping the FenFit output image from the 2D parameterized mesh to the 3D graft surface. Given the mesh generated under the discrete Laplacian transformation is tetrahedral, barycentric coordinates were proposed to discretize and interpolate the FenFit image across the graft surface. Barycentric coordinates have applications in computer graphics [26], video games [33], and recently, medical imaging diagnostics and segmentation [30]. Under a barycentric coorindate system, the location of a point within a triangle in 3D space is defined as a sum of weights or "masses" located at its vertices, as illustrated in Figure 4-8. The coordinate system can be thought of as the "centre of mass" of 3 point masses placed at each vertex of triangle.

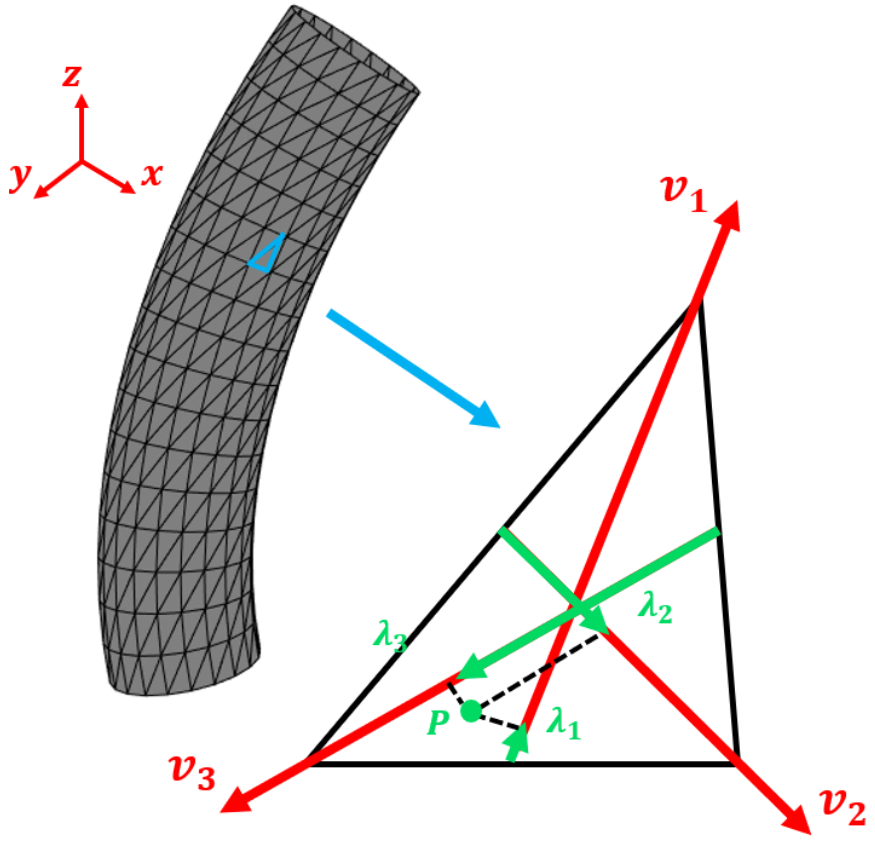

Figure 4-8: **Barycentric coorindate system for a given triangular mesh face**. The point P in the 3D cartesian space (x, y, z) is expressed in terms of the barycentric coorindates $(\lambda_1, \lambda_2, \lambda_3)$

To discretely interpolate the FenFit output image across the graft's surface, we can write the Cartesian coordinates of a point r on the graft's surface as a function of both the barycentric coordinates and the local triangular vertices.

$$x = \lambda_1 x_1 + \lambda_2 x_2 + \lambda_3 x_3 \tag{4.8}$$

$$y = \lambda_1 y_1 + \lambda_2 y_2 + \lambda_3 y_3 \tag{4.9}$$

Where x and y define a point bounded within the triangular vertices $(x_1, y_1), (x_2, y_2)$, and (x_3, y_3), and λ_1, λ_2, and λ_3 are the barycentric coorindates that sum to $\lambda_1 + \lambda_2 + \lambda_3 = 1$. All weights must sum to unity to ensure the final result obtained is contained within the bounds of the triangle. Note that locally on the surface of the graft, we can assume the mesh is flat and approximately 2 dimensional.

For our application, we require an inverse mapping of equations 4.9 above; that is, a transformation that converts (x, y) coordinates on the FenFit image to a barycentric coordinates suitable for rendering in the 3D graft space. To obtain such a transformation, we first rearrange the identity $\lambda_1 + \lambda_2 + \lambda_3 = 1$, and substitute into Equation 4.9 above,

$$x - x_3 = \lambda_1(x_1 - x_3) + \lambda_2(x_2 - x_3) \tag{4.10}$$

$$y - y_3 = \lambda_1(y_1 - y_3) + \lambda_2(y_2 - y_3) \tag{4.11}$$

Or in matrix form,

$$r - r_3 = T\lambda \tag{4.12}$$

Where,

$$T = \begin{bmatrix} x_1 - x_3 & x_2 - x_3 \\ y_1 - y_3 & y_2 - y_3 \end{bmatrix}$$

Finally, to obtain the desired mapping, we invert the matrix T,

$$\lambda = T^{-1}(r - r_3) \tag{4.13}$$

Where, explicitly, the components of T^{-1} can be calculated by,

$$\lambda_1 = \frac{(y_2 - y_3)(x - x_3) - (x_3 - x_2)(y - y_3)}{\det(T)} \tag{4.14}$$

$$\lambda_2 = \frac{(y_3 - y_1)(x - x_3) - (x_1 - x_3)(y - y_3)}{\det(T)} \tag{4.15}$$

To implement the equations above in practice, each triangular mesh face was first discretized into barycentric coordinates using 4.15. For each face on the deformed 2D mesh, its corresponding 3D vertices was extracted, and a 1-1 mapping was assigned between pixels on the 2D face's image segment, and their corresponding barycentric coordinates in 3D space. Finally, the image element was interpolated across the graft's surface, according to each pixel's mapping under the barycentric coordinate system. Final results obtained from the texture mapping algorithm, and visualization algorithm as a whole, are illustrated in Figure 4-9. Note that bifurcated graft legs would be introduced in the case of an aneurysm that lies close to the femoral arteries, though these additional legs have no effect on the fit of the visceral vessels.

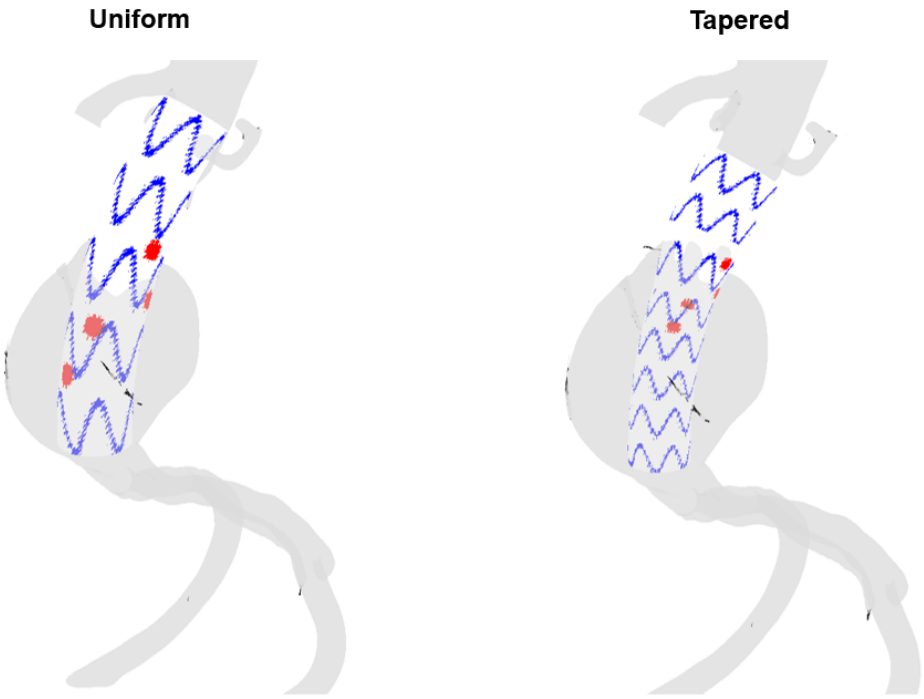

Figure 4-9: Sample outputs from FenFit's 3D visualization function for uniform and tapered graft geometries. The aligned fenestration locations are highlighted in red.

Chapter 5

Conclusions and Future Work

This thesis aimed to use computational tools and a deterministic clinical design process to optimize treatment for acute endovascular and respiratory conditions.

A low-cost, rapidly deployable emergency ventilator design using a novel fluidic oscillator was developed. A CFD model was used to assess flow characteristics of the system, and a prototype was developed and tested with a commercial benchtop respiratory stimulator. The simulations showed clinically relevant periodic oscillations and outlet pressures. Both the prototype and simulations responded promptly to disrupted oscillations, an analogue for patient-initiated breaths.

At the time of writing, the COVID-19 pandemic continues to pose an alarming threat in many developing countries around the world. India reported over 300,000 new cases daily during the period from April 21st to April 30th 2021 [3]. We do not envision use of our ventilator design when fully electronic, commercial ventilators are available that offer on-demand, digital control of clinical parameters and multiple modes of ventilation (pressure-controlled and volume-controlled). We recommend oscillator use primarily as an emergency ventilator where there may be no other ventilator options available, due to cost, demand, or lack of electricity (which is often the case in healthcare settings for many developing countries).

We believe our technology could have many other applications as a cheap fluidic control system, offering an alternative over more expensive electronic microcontroller systems. For example, recently, our group has developed a mechanical diaphragmatic

assist device for treatment of various respiratory pathologies that use oscillatory soft robotic actuation to augment native breathing mechanics [15]. This system could benefit from a fluidic oscillator design that can achieve relevant respiratory rates while being small enough to be easily implantable without an external power source. Moreover, our device can also be easily connected to a set of animal lungs, which may provide a low-cost simulation platform and educational tool for respiratory medical devices (similar to our group's showcase at the "Plastic" convention in Science Gallery Dublin 2019 [16]).

An automated program for aligning patient-specific aortic fenestrations along endovascular grafts was developed. An intuitive user interface was designed for inputting patient anatomy, locating a valid alignment, and reporting of results. A rendering algorithm for mapping the alignment selection to a 3D visualization of the graft was also explored. Results visualization should improve physician confidence in the program, which, hopefully, in turn will expedite widespread adoption.

FenFit has been shown to reduce case planning time by 22 minutes, and improve accuracy in 48% of clinical trial cases. Assuming a total operating room cost of \$2200/hr and 7000 annual fenestrated endovascular repair cases [8], FenFit could offer over \$5 million dollars in savings to the national healthcare system annually. Given the potential cost savings offered to hospitals by our program, a number of medical imaging companies have expressed interest in collaborating with our group to commercialize FenFit, and potentially integrate with their existing software. These companies include Terarecon, Philips, Gore, 3mensio, and Cook Medical, who may help to expedite FDA approval for FenFit moving forward. Moreover, we believe FenFit is scalable, and can be expanded to treat almost all aneurysm types (thoracic, femoral, carotid etc.). To date, a provisional patent application has also been filed with MIT's Technology Licensing Office.

At the time of writing, clinical testing of FenFit is still underway at BIDMC. We see a number of opportunities moving forward to further improve the accuracy and efficiency of fenestration case planning and treatment:

1. Auto-segmentation of CT scans and extraction of the PGD and AL locations using a 3D segmentation software package could be achieved using supervised machine learning techniques. AI algorithms may also be implemented in future studies of automated graft selection.

2. Combining the output of FenFit with FEA / CFD modelling could allow the physician to maximise durability of the graft while simultaneously, while ensuring patency of the fenestrations. To account for aortic bending imposed through endograft deployment, vessel straightening effects may be modelled to predict the post-operative aortic shape (similar to the methods employed in [50]).

3. To automate the final workflow step outlined in Figure 3-3, the output of FenFit could be fed to a subtractive manufacturing device (e.g. a laser cutter) for precise, automated modification of off-the-shelf endografts.

4. Surgical robotic technologies are becoming increasingly employed in the field of vascular surgery [40], [11]. Conducting FenFit based on *in situ* AL and PGD measurements and automatically fenestrating the graft *a posteriori* and *in situ* has the potential to greatly reduce the time and effort required for graft deployment, while simultaneously improving alignment accuracy.

Integration of all the components above would provide the physician with a fully automated workflow, starting with the CT scan, and finishing with an implanted endograft. The entire process could be completed in just a few minutes, freeing up hospital resources, and reducing operative time and costs.

The use of computational modeling and a deterministic design process facilitated rapid, low-cost prototyping in this thesis. Computational and analytical tools are becoming increasingly utilized by engineers in the MedTech industry, who wish to avoid a more expensive and time-consuming "shoot-the-dark" design process. Both of the projects discussed in this thesis propose expedited, customized treatment for urgent medical conditions, which will hopefully translate to improved clinical outcomes and reduced fatality rates.

Appendix A

Appendix A

A.1 Oscillator Dimensions

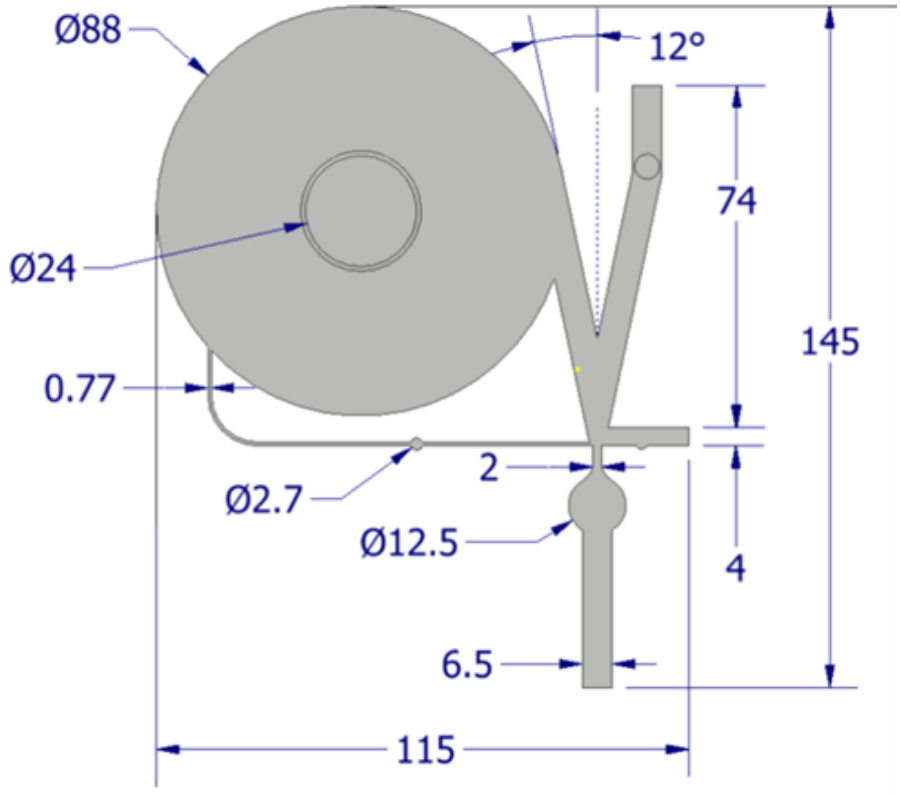

Figure A-1: Fluidic Oscillator Dimensions

Bibliography

[1] B. S. Brook D. Breen A. W. Miles D. G. Tilley A. J. Wilson, C. M. Murphy. Med. eng. phys., 2009. 13504533.

[2] Mohsen Bannazadeh, William E. Beckerman, Adam H. Korayem, and James F. McKinsey. Two-year evaluation of fenestrated and parallel branch endografts for the treatment of juxtarenal, suprarenal, and thoracoabdominal aneurysms at a single institution, jan 2020.

[3] Anoo Bhuyan. Experts criticise India's complacency over COVID-19, May 2021. doi: 10.1016/S0140-6736(21)00993-4.

[4] Mayo Clinic. Endovascular repair of complex aortic aneurysms, cardiovascular diseases. https://www.mayoclinic.org/medical-professionals/cardiovascular-diseases/.

[5] P. Sah A. Shoukat A. Pandey A. M. El-Sayed B. H. Singer S. M. Moghadas A. P. Galvani C.R Wells, M. C. Fitzpatrick. Lancet infect. dis., 2020. 14744457.

[6] Doyle M.G. Leonard W. T. Crawford, S.A. 'in-stock' fenestrated stent graft for the urgent repair of an abdominal aortic aneurysm, May 2016.

[7] M. Stearn-Hassenpflug D. C. Chao, D. J. Scheinhorn. Chest, 1997. 00123692.

[8] Kirsten D. Dansey, Rens R.B. Varkevisser, Nicholas J. Swerdlow, Chun Li, Livia E.V.M. de Guerre, Patric Liang, Christina Marcaccio, Thomas FX. O'Donnell, Brett J. Carroll, and Marc Schermerhorn. Epidemiology of Endovascular and Open Repair for Abdominal Aortic Aneurysms in the United States from 2004-2015 and Implications for Screening, Feb 2021.

[9] Mathieu Desbrun, Mark Meyer, and Pierre Alliez. Intrinsic Parameterizations of Surface Meshes, 2002.

[10] L. Brochard C. S. Calfee N. D. Ferguson A. S. Slutsky D. Brodie E. Fan, J. R. Beitler. Lancet respir. med, 2020.

[11] Pierre G. S. Jian S. D. Daniel M. Helge A. W. Estevan H.M., Shervanthi H.V. Towards a modular suturing catheter for minimally invasive vascular surgery.

[12] Alice Fantazzini, Mario Esposito, Alice Finotello, Ferdinando Auricchio, Bianca Pane, Curzio Basso, Giovanni Spinella, and Michele Conti. 3D Automatic Segmentation of Aortic Computed Tomography Angiography Combining Multi-View 2D Convolutional Neural Networks, oct 2020.

[13] L. Blanch G. Murias, U. Lucangelo. Curr. opin. crit. care. 15317072.

[14] ANSYS Fluent User's Guide. Ansys, 2017.

[15] Markus A. Horvath, Lucy Hu, Tanja Mueller, Jon Hochstein, Luca Rosalia, Kathryn A. Hibbert, Charles C. Hardin, and Ellen T. Roche. An organosynthetic soft robotic respiratory simulator, June 2020.

[16] Rosalia L. Roche E.T. Horvath M., Hu L. Plastic conventioncant live with it, can't live without it, 2019. retrieved at: https://www.irishtimes.com/culture/plastic-the-many-good-uses-of-a-vilified-modern-material.

[17] M. K. Hurdal, K. W. Kurtz, and D. C. Banks. Case study: Interacting with cortical flat maps of the human brain, 2001.

[18] J. K. Royle J. R. Tippetts, H. K. Ng, 1973.

[19] J. W. Joyce. The army emergency respirator, 1968.

[20] R. McNeill S. Granados K. Houreld, D. Lewis. Virus exposes gaping holes in africa's health systems, 2020.

[21] W. Kabsch. A discussion of the solution for the best rotation to relate two sets of vectors, Sep 1978. Acta Crystallographica.

[22] R. M. Kacmarek. Egan's fundamentals of respiratory care, the c.v. mosby company, 1990.

[23] Rashed Karim, Yingliang Ma, and Jang. Surface flattening of the human left atrium and proof-of-concept clinical applications, 2014.

[24] K. Craig Kent. Deployment of an endovascular graft in an abdominal aortic aneurysm, 2014.

[25] A. Pesenti L. Bigatello. Anesthesiology 2019, 2019. 15281175.

[26] Philippe B Laval. Mathematics for Computer Graphics-Barycentric Coordinates, 2003.

[27] Bruno Levy. Parameterization of mesh-models, jun 2006. Association for Computing Machinery (ACM).

[28] Society of Vascular Surgery M. J. Singh. Abdominal aortic aneurysm. retrieved at: vascular.org/patient-resources/vascular-conditions.

[29] Cook Medical. Zenith endovascular grafts, physician's pocket guide"=. retrieved at: https://www.cookmedical.com/products/.

[30] Dana M. Middleton, Jonathan Y. Li, Hui J. Lee, Steven Chen, Patricia I. Dickson, N. Matthew Ellinwood, Leonard E. White, and James M. Provenzale. Diffusion tensor imaging tensor shape analysis for assessment of regional white matter differences, Aug 2017.

[31] Toshifumi Mita, Takeshi Arita, Naofumi Matsunaga, Matakazu Furukawa, Nobuya Zempo, Kensuke Esato, and Masunori Matsuzaki. Complications of endovascular repair for thoracic and abdominal aortic aneurysm: An imaging spectrum, sep 2000.

[32] K. Moerman. GIBBON: The Geometry and Image-Based Bioengineering Add-On, February 2018. doi:10.21105/joss.00506.

[33] Benedek Nagy and Khaled Abuhmaidan. A continuous coordinate system for the plane by triangular symmetry, feb 2019.

[34] G N Newsam. Some Topical Variational Geometry Problems in Computer Graphics, jan 1991.

[35] Kikinis R. Pieper S, Halle M. 3d slicer, 2004. Proceedings of the 1st IEEE International Symposium on Biomedical Imaging: From Nano to Macro.

[36] Ulrich Pinkall and Konrad Polthier. Computing discrete minimal surfaces and their conjugates, 1993.

[37] S. E. Buchalter R. B. Gammon, M. S. Shin.

[38] R. M. Kacmarek R. Goulet, D. Hess. Chest, 1997. 00123692.

[39] AAMI Concensus Report. Emergency use ventilator (euv) design guidance, 2020.

[40] Celia V. Riga, Colin D. Bicknell, Alexander Rolls, Nicholas J. Cheshire, and Mohamad S. Hamady. Robot-assisted fenestrated endovascular aneurysm repair (FEVAR) using the magellan system, feb 2013.

[41] Yusuke S. Ryosuke S. Experimental Study on Relationship between Indices of Network Structure and Spectral Distribution of Graphs, 2016.

[42] A. S. Slutsky. Chest, 1993.

[43] G. Strang. Computational science and engineering, 2007. Wellesley, Cambridge Press.

[44] Frost Sullivan. Hidden health crisis costing america billions, 2016.

[45] Columbia Surgery. Aortic aneurysms. retrieved at: columbiasurgery.org/aortic-aneurysms.

[46] Nicholas J. Swerdlow, Winona W. Wu, and Marc L. Schermerhorn. Open and endovascular management of aortic aneurysms, 2019.

[47] Dillon T., Ozturk C., Mendez K., Rosalia L., Gollob S., Kempf K., and Roche E.T. Computational Fluidic Modeling of a Low-Cost Fluidic Oscillator for Conversion of a CPAP Machine into an Emergency Use Mechanical Ventilator. *Advanced NanoBiomed Research*, Jan 2021.

[48] E. Smyk V. Tesař, K. Peszynski. Epj web conf., 2016. 2100014.

[49] Michael E Wall, Andreas Rechtsteiner, and Luis M Rocha. Singular value decomposition and principal component analysis, 2003.

[50] Inoue K. Yoshino D., Sato M. Estimation of force on vascular wall caused by insertion of self-expanding stents. J. Engineering in Medicine.

[51] Hao Zhang, Oliver Van Kaick, and Ramsay Dyer. Spectral Mesh Processing, 1981.

[52] Jiechang Zhu, Lujing Zhao, and Dai. Fenestrated Thoracic Endovascular Aortic Repair Using Physician Modified Stent Grafts for Acute Type B Aortic Dissection with Unfavourable Landing Zone, feb 2018.